Correspondence to:

A. Bier,
andreas.bier@dlr.de

Impact of Parametrizing Microphysical Processes in the Jet and Vortex Phase on Contrail Cirrus Properties and Radiative Forcing

A. Bier[1] and **U. Burkhardt[1]**

[1]Deutsches Zentrum für Luft- und Raumfahrt, Institut für Physik der Atmosphäre, Wessling, Germany

Abstract Contrail ice nucleation and ice crystal loss during the vortex phase control ice crystal numbers in young contrails and can have a strong impact on the properties and the life cycle of contrail cirrus. For current soot number emissions, ice nucleation is controlled by the number of emitted soot particles and atmospheric conditions while the vortex phase loss depends predominantly on the nucleated ice crystal numbers and the ambient relative humidity. Initial ice crystal numbers after the vortex phase are close to the emitted soot particle number only for very low ambient temperatures (<210 K) and for highly ice-supersaturated conditions. Higher temperatures and lower relative humidities lead to significantly decreased ice crystal numbers. Global climate model simulations show that initial contrail ice crystal numbers per fuel mass are on average 50%–65% decreased relative to the soot number emission index in the extratropics and more in tropics. In the extratropics, this is mainly caused by a high ice crystal loss during the vortex phase and in the (sub)tropics and at lower flight levels by decreased ice nucleation. Simulated ice crystal numbers per newly formed contrail length agree well with in situ measurements over central Europe within the variability of present-day soot number emissions. Our estimated global mean contrail cirrus radiative forcing (RF) for the year 2006 is 44 (31–49) mWm^{-2}, around 22% lower than estimated in a previous study. When reducing soot number emissions by 80%, RF decreases by 41%, slightly less than suggested by a recent study.

Plain Language Summary Contrail cirrus are known to be a major contribution to the aviation climate impact connected with a large uncertainty. Earlier research has shown that the ice crystal number in newly formed contrails has a large impact on the average contrail cirrus climate impact. But the properties of newly formed contrails are not well captured within the climate models. We have improved the representation of the contrail formation processes in our contrail cirrus module within the ECHAM climate model by including parameterizations for contrail ice nucleation and the ice crystal survival in the vortex phase. We could show that young contrail properties agree well with available campaign measurements over central Europe, given the large variability in soot number emissions, when matching geographical locations, cruise level, and atmospheric variables. The improvements within our contrail cirrus parameterization lead to a decrease in our estimate of contrail cirrus radiative forcing by slightly more than 20% relative to our earlier estimates in which we prescribed constant initial ice crystal numbers. Furthermore, our improved model indicates that the decrease in the contrail cirrus climate impact due to introducing biofuels, which lead to a decrease in soot number emissions, is slightly smaller than estimated earlier.

1. Introduction

In the year 2011, aviation contributed around 3.5% to the anthropogenic climate forcing (Lee et al., 2021). Assuming no change in aircraft technology or fuel, the climate impact of aviation is expected to increase due to yearly growth of revenue passenger kilometers by 5% (International Civil Aviation Organization, 2013). The radiative forcing (RF) due to contrail cirrus is larger than that due to CO$_2$ emitted by aircraft and accumulated since the beginning of air traffic (e.g., Bock & Burkhardt, 2016a; Boucher et al., 2013; Burkhardt & Kärcher, 2011) and is set to increase threefold until 2050 (Bock & Burkhardt, 2019). The uncertainty in the estimates of contrail cirrus RF is high, partly due to uncertainties in the contrail cirrus parameterizations applied in global climate models (Lee et al., 2021).

Contrails form when water saturation is reached or surpassed within the aircraft plume due to mixing of the hot and moist exhaust air with the cold ambient air (Schumann, 1996). During the jet phase, emitted engine soot particles and ambient particles entrained from the environment activate into water droplets and subsequently

freeze to ice crystals by homogeneous nucleation. The number of nucleated ice crystals depends on engine and fuel parameters as well as on the ambient atmosphere (Kärcher et al., 2015) and displays large regional variations (Bier & Burkhardt, 2019). In the subsequent vortex phase, the exhaust particles and contrail ice crystals are trapped in a pair of descending counter-rotating vortices forming the primary wake (Paoli & Shariff, 2016). The adiabatic heating during the descent of the vortex pair causes a decrease in relative humidity. This may lead to ice-subsaturated air inside the vortices and, therefore, to the sublimation and eventually to a possible loss of trapped ice crystals (Lewellen & Lewellen, 2001; Sussmann & Gierens, 1999). Some ice crystals (typically a fraction of 10%–30%) are continuously detrained from the primary wake and rise due to buoyancy (Gerz et al., 1998). They make up a curtain between the primary wake and the original emission altitude. During the dispersion regime after vortex breakup, contrail evolution is controlled by the exchange with the ambient atmosphere. Important processes are the horizontal spreading due to vertical wind shear, advection, volume growth due to turbulent diffusion, ice water deposition, and sedimentation of ice crystals (e.g., Bier et al., 2017; Bock & Burkhardt, 2016b; Schumann & Heymsfield, 2017).

Several studies estimated the global mean radiative forcing due to contrail cirrus by applying general atmospheric circulation models. Based on the contrail cirrus parameterization of Burkhardt and Kärcher (2009) within the ECHAM5 climate model, Burkhardt and Kärcher (2011) calculated a RF of 37 mWm^{-2} for the year 2002. With the extension of this contrail cirrus parameterization to the microphysical two-moment scheme of Lohmann et al. (2008), Bock and Burkhardt (2016a) estimated a RF of 35 mWm^{-2} using the AERO2k flight inventory representative for the year 2002 (Eyers et al., 2004) and of 56 mWm^{-2} using the Aviation Environmental Design Tool (AEDT) flight inventory for 2006 (Wilkerson et al., 2010). This increase in the RF by 60% from 2002 to 2006 results, on the one hand, from the increase in air traffic and, on the other hand, from a more realistic representation of the flight distance in the AEDT inventory. Schumann et al. (2015) estimated the RF to be around 60 mWm^{-2} for 2006 by means of a contrail cirrus prediction model (CoCiP) coupled with the Community Atmospheric Model (CAM3). Chen and Gettelman (2013) determined a RF of 13 mWm^{-2} with the Community Atmosphere Model (CAM5). After a correction of the initial contrail ice crystal sizes and of the initial contrail cross-sectional area, this value was later updated to a RF of 57 mWm^{-2} (Lee et al., 2021).

A major uncertainty when estimating the RF comes from the contrail cirrus induced cloud feedback. This is because the atmospheric humidity is depleted due to water vapor deposition on contrail ice crystals, which may suppress the formation of natural cirrus. Burkhardt and Kärcher (2011) estimated this negative feedback for cirrus clouds to be around 20% of the RF. In a more comprehensive study, Bickel et al. (2020) estimated the global Effective Radiative Forcing (ERF) due to contrail cirrus by analyzing the complete set of rapid radiative adjustments induced by contrail cirrus. They find that the ERF is reduced by 60%–70% relative to the RF, which, however, required 12 times scaling of air traffic to yield convincing statistical significance of the results. RF may be converted into ERF by a factor (Bickel et al., 2020; Lee et al., 2021) with a possibly large but as yet unknown increase in uncertainty (Lee et al., 2021) and both parameters are closely depending on each other (Ponater et al., 2021).

Current climate model studies of the properties and radiative impact of contrail cirrus (Bock & Burkhardt, 2016a; Burkhardt & Kärcher, 2011; Chen & Gettelman, 2013; Schumann et al., 2015) do not or only partly consider the impact of the variability in initial contrail ice crystal numbers. (Note that we refer "initial" to contrails of several minutes of age and after the vortex phase in the present study). In the tropics and at lower flight levels in the subtropics, atmospheric conditions close to the contrail formation threshold limit contrail ice nucleation (Bier & Burkhardt, 2019). Furthermore, ice crystal loss within the vortex phase leads to a significant reduction in ice crystal numbers that can vary with geographical region and altitude. Neglecting these processes may lead to a significant overestimation of contrail cirrus ice number concentrations, optical thickness, coverage, as well as lifetime and RF in those areas. In this study, we include parameterizations of contrail ice nucleation (Kärcher et al., 2015) and of the ice crystal loss during the vortex phase (Unterstrasser, 2014) within the contrail cirrus scheme CCMod of the global climate model ECHAM5. Our objective is to analyze the combined effect of these two processes on initial contrail ice crystal numbers and contrail cirrus properties (averaged over all ages) and their variation with atmospheric conditions and soot number emissions. We compare our calculated RF for the year 2006 with the recent estimate by Bock and Burkhardt (2016a) who prescribed spatially and temporally constant initial ice crystal numbers. We also revisit the previous estimates of the impact of a reduction in soot number emissions on RF (Burkhardt et al., 2018).
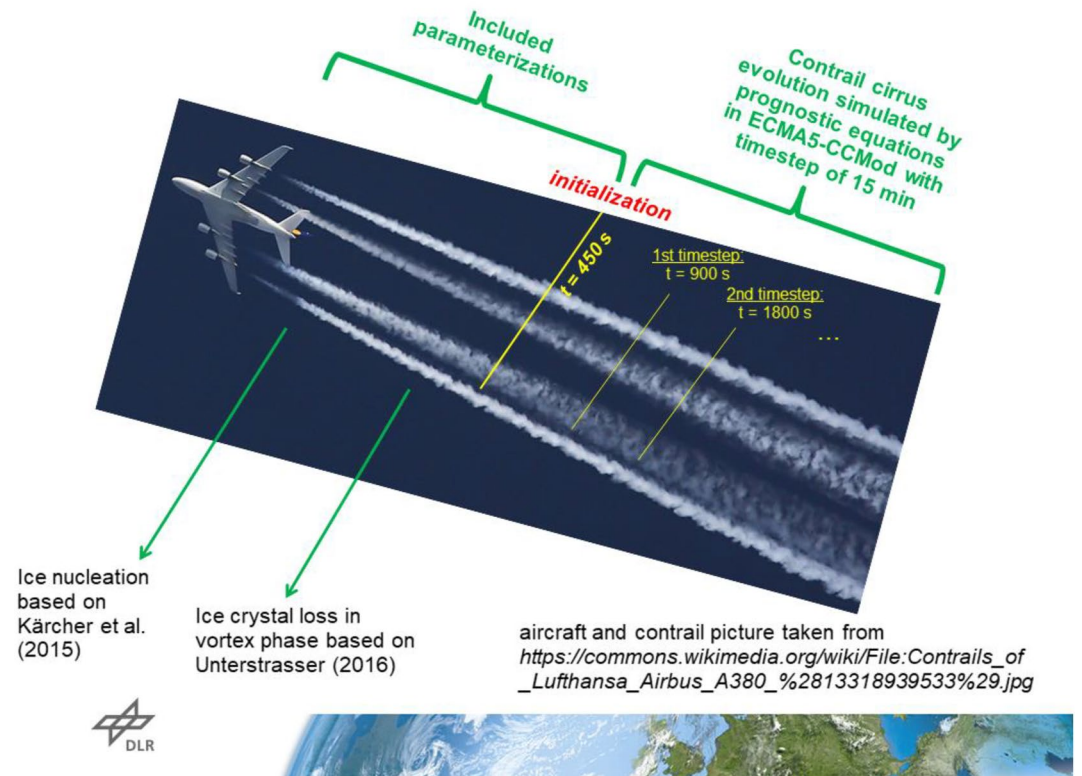
Figure 1. Contrail stages and their treatment in the global climate model ECHAM5-CCMod. The aircraft and contrail picture is taken from https://commons.wikimedia.org/wiki/File:Contrails_of_Lufthansa_Airbus_A380_%2813318939533%29.jpg and can be used according to the Attribution-Share Alike 2.0 Generic license.

In Section 2, we describe the climate model ECHAM5-CCMod which includes a contrail cirrus module comprising a microphysical two-moment scheme (Bock & Burkhardt, 2016b). We give an overview over our calculations, investigating offline the dependence of ice nucleation and ice crystal loss during the vortex phase on the atmospheric state and soot number emissions, and our general circulation model simulations. In Section 3, we investigate the combined effect of ice nucleation and vortex phase loss on contrail ice crystal numbers depending on atmospheric parameters and soot number emissions in an offline study. In Section 4, we analyze the spatial variability in contrail ice nucleation and ice crystal loss during the vortex phase and evaluate the resulting ice crystal numbers in young contrails with in situ measurements and observations over central Europe accounting for the variability in present-day soot number emissions. We describe in Section 5 the spatial distribution of contrail cirrus microphysical properties and coverage and provide an estimate of global contrail cirrus RF. Finally, in Section 6, we analyze the impact of the soot number emissions on young contrail ice crystal numbers, contrail cirrus properties, and the RF. Conclusions and outlook are given in Section 7.

2. Methods

We use the ECHAM5-HAM model with a two-moment microphysical scheme that was extended to include a new cloud class, that is, contrail cirrus (Section 2.1). So far, contrail cirrus were initialized using a fixed ice crystal number based on observations over Europe (Bock & Burkhardt, 2016a). In the present study, we extend the contrail cirrus module by adding a parameterization for contrail ice nucleation in the jet phase (Section 2.1.2) and a parameterization of the ice crystal loss in the vortex phase (Section 2.1.3), respectively, and, hence, enable the contrail ice crystal number to vary already at initialization depending on soot number emissions and atmospheric conditions. We describe the initialization of contrails at an age of 450 s (representing half of a model time step) in Section 2.1.4. The included parameterizations and the contrail initialization time are displayed in a simplified scheme (Figure 1). Estimates for current soot number emissions are discussed in Section 2.2. We introduce our

offline studies to ice nucleation and vortex phase survival in Section 2.3 and the climate model simulations in Section 2.4.

2.1. ECHAM5-CCMod

Our simulations are performed with the atmospheric general circulation model ECHAM5 (Roeckner et al., 2003, 2006), which has been extended by the Hamburg Aerosol Module (HAM, Stier et al., 2005). The contrail cirrus parameterization follows Burkhardt and Kärcher (2009), who introduce contrail cirrus as a separate cloud class in addition to natural cirrus clouds. Ice water content, contrail coverage, and length of contrail cirrus are calculated as prognostic variables depending on persistence, advection, spreading, and deposition/sublimation. Contrails form according to the Schmidt-Appleman (SA)-criterion (Schumann, 1996), described in Section 2.1.1, and persist in the ice-supersaturated but cloud-free part of the model grid box, which is parametrized consistent with the natural cloud scheme (Burkhardt et al., 2008). Bock and Burkhardt (2016b) extended the contrail cirrus parameterization (CCMod) of Burkhardt and Kärcher (2009) using a microphysical two-moment scheme (Lohmann et al., 2008). Contrail cirrus ice crystal number concentration and volume are introduced as additional prognostic variables. This leads to a better representation of microphysical processes and is essential for mitigation studies regarding the influence of aircraft particle number emissions on contrail cirrus properties and their climate impact. The cloud water content in ECHAM5 usually grows assuming saturation adjustment. In cases of contrail cirrus volumes with very low ice crystal number concentrations, as they may occur for aged contrails in connection with enhanced ice crystal sedimentation, ice water deposition is limited using the diffusional growth equation described in Bock and Burkhardt (2016b).

2.1.1. Contrail Formation Criterion

The SA-criterion is purely derived from plume thermodynamics (Schumann, 1996). Behind the engine exit, the hot and moist plume exhaust air continuously mixes with the colder ambient air and, finally, approaches atmospheric conditions. This can be characterized by a "mixing line" describing the linear dependency between partial vapor pressure and temperature in a plume. The SA-criterion is fulfilled if the mixing line crosses the water saturation vapor pressure so that plume relative humidity over water exceeds water saturation and, hence, exhaust particles can activate into water droplets and subsequently freeze to ice crystals. This criterion is validated by a majority of flight campaigns that have shown that visible contrails only form if the plume exceeds water saturation. The threshold for contrail formation occurs when the mixing line just touches the saturation vapor pressure. While the osculation point defines the threshold temperature at water saturation θ_{100}, the SA-threshold temperature θ_G (i.e., the largest possible ambient temperature for contrail formation) is obtained by following the mixing line from water saturation to the current atmospheric relative humidity over water. Since the upper troposphere is in general water-subsaturated, θ_G is typically several K below θ_{100} and decreases with decreasing ambient relative humidity. Furthermore, θ_G is controlled by the slope of the mixing line which is determined by fuel/engine properties (i.e., specific combustion heat, propulsion efficiency, and water vapor mass emission index) and the air pressure. For conventional passenger aircraft, θ_G typically ranges between around 220 and 230 K. Further details regarding the SA-criterion and its uncertainty are described in Schumann (1996). For both offline studies and climate model simulations, we prescribe fuel/engine properties that influence the contrail formation threshold according to Schumann (1996).

2.1.2. Parametrized Contrail Ice Nucleation

As described in Bier and Burkhardt (2019), we have included the contrail ice nucleation parametrization by Kärcher et al. (2015) within ECHAM5-CCMod. While Bier and Burkhardt (2019) describe this parameterization in more detail, we here provide a short summary for the basic approach: The plume cools with increasing time due to continuous mixing of the exhaust with ambient air and eventually becomes water-supersaturated if the SA-criterion is fulfilled. The number of activated aerosol particles originating from soot and ambient particles is calculated depending on ambient conditions, fuel/engine, and the exhaust particle properties. The final droplet number concentration (n_o) is calculated from the condition that the condensational loss that is connected with the formation of droplets prevents any further increase in relative humidity over water. Therefore, the condensational loss depending on the concentration of emitted and ambient aerosol particles needs to balance the increase in relative humidity due to the plume dilution. The parameterization assumes that all droplets form at the same time, denoted by the subscript o, and that these droplets grow due to condensation and subsequently freeze rapidly into

ice crystals by homogeneous nucleation. Hence, the nucleated ice crystal number concentration is approximated by n_o.

The number of ice crystals nucleating in the plume is strongly dependent on the difference between the ambient temperature and the contrail formation threshold temperature. For soot-rich emissions and at ambient temperatures of several K below the contrail formation threshold, ice nucleation is mainly controlled by soot number emissions (Kärcher, 2018; Kärcher & Yu, 2009). The apparent ice number emission index after nucleation (the number of formed ice crystals per mass of burnt fuel) is given by the following equation:

$$AEI_{nuc} = \frac{n_o C_o}{\rho_o},$$ (1)

where C_o and ρ_o denote the air-to-fuel ratio (dilution) and the plume air density at the time of droplet formation, respectively. For soot-rich emissions, AEI_{nuc} is approximately equal to the fraction of soot particles forming ice crystals multiplied with the soot number emission index (EI_s). For lower soot number emissions and at atmospheric conditions very close to the formation threshold, the number of background aerosol particles entrained into the plume becomes more relevant for ice nucleation (e.g., Bier & Burkhardt, 2019).

The parameterization of Kärcher et al. (2015) uses the solubility model from Petters and Kreidenweis (2007) describing the activity of water in a solution as a function of volume of water and dry particulate matter, respectively, and a single hygroscopicity parameter κ. Including the Kelvin term yields the "κ-Köhler theory" which defines the saturation ratio of a solution droplet depending on the particle dry core radius and hygroscopicity. Note that we have modified the parameterization of Kärcher et al. (2015) by adapting the calculation of the activation dry core radius of soot particles due to the low hygroscopicity of these particles. Details are described in Appendix A.

2.1.3. Parametrized Ice Crystal Loss During the Vortex Phase

Unterstrasser (2016) calculates the number of contrail ice crystals surviving the vortex phase for given numbers of formed ice crystals. He developed a parameterization of ice crystal loss within the vortex phase (Unterstrasser, 2014; Unterstrasser & Görsch, 2014) by means of the 3D Large Eddy Simulations (LES) model EULAG (Smolarkiewicz & Grell, 1992), which is fully coupled with the particle based Lagrangian Cloud Module (LCM; Sölch & Kärcher, 2010). These simulations start at a plume age of several seconds when ice nucleation and the roll-up of the wake vortices are expected to be finished.

The number of ice crystals surviving the vortex phase is dependent on ambient temperature, relative humidity over ice, the number of nucleated ice crystals, Brunt-Vaisälä frequency, the weight and wing span of the aircraft, and the water vapor emission. Unterstrasser (2016) developed a parameterization for the fraction of ice crystals surviving the vortex phase, the so-called "survival fraction" (f_N), by systematic variation of those variables. He introduces three characteristic length scales to characterize the processes in the downward sinking contrail, namely for (a) the final vertical displacement of the wake vortex and (b) the effect of ambient relative humidity and (c) of the emitted engine water vapor on the ice crystal budget. Thereby, the simulated f_N are approximated by an arc tangent functional relationship that solely depends on a linear combination of the three length scales. The vertical displacement needed for reaching ice saturation is compared with the vertical displacement of the wake vortex and finally the number of sublimating ice crystals is calculated in those areas of the wake vortices where ice-subsaturated conditions prevail.

The sensitivity of the ice crystal survival to the aircraft wing span was explored by Unterstrasser (2016). A larger wing span is typically associated with a heavier aircraft that develops stronger wake vortices. He shows that in particular for low to moderate ice-supersaturations the vortex phase loss increases significantly with increasing aircraft size. For the calculation of the ice crystal loss during the vortex phase, we only consider the dependencies, connected with the variability of the ambient temperature, relative humidity over ice, and the number of nucleated ice crystals in the present study. Since we have no information on the aircraft type associated with the flight inventory, we assume a fixed wing span of 50 m as a typical average aircraft fleet value. The Brunt-Väisälä frequency is fixed to 0.01 s^{-1} (= 1/s), a common value in the upper troposphere.

We implemented this parameterization in ECHAM5-CCMod accounting for the variability in the main (not aircraft-specific) parameters controlling the survival fraction. As a measure for the number of ice crystals

surviving the vortex phase per burnt fuel mass, we introduce the "apparent ice number emission index after the vortex phase":

$$\text{AEI}_{\text{ice}} = f_{\text{N}} \cdot \text{AEI}_{\text{nuc}}. \tag{2}$$

2.1.4. Initial Contrail Properties

We calculate the contrail ice crystal number concentration (n_{co}) and the cross-sectional contrail area (A_{co}) for a plume age at which contrails are initialized in ECHAM5-CCMod ($t_{\text{ini}} = 450$ s).

We determine n_{co} by assuming a continuous dilution of the exhaust plume starting at the time of contrail formation and including the ice crystal loss during the vortex regime:

$$n_{\text{co}}(t_{\text{ini}}) = n_o \cdot \frac{D(t_{\text{ini}})}{D_o} \cdot \frac{\rho(t_{\text{ini}})}{\rho_o} \cdot f_{\text{N}}, \tag{3}$$

where n_{o}, D_{o}, and ρ_{o} are the ice crystal number concentration, the dilution factor, and the plume air density at the time of contrail formation (all obtained from the parameterization of Kärcher et al., 2015), respectively, and $\rho(t_{\text{ini}})$ is the plume air density at t_{ini}. We approximate $\rho(t_{\text{ini}})$ by the ambient air density since plume temperatures have almost decreased to ambient temperature after 450 s. The plume dilution factor is defined as the quotient between the dilution at the engine exit (C_{e}) and the dilution at a certain plume age so that $D(t_{\text{ini}}) = C_{\text{e}}/C(t_{\text{ini}})$. We set $C_{\text{e}} = 70$ as a typical value for commercial aircraft and being consistent with a plume exit temperature of approximately 600 K (Bier et al., 2022).

The contrail cross-sectional area is obtained from mass conservation (Schumann et al., 1998) as follows:

$$A_{\text{co}}(t_{\text{ini}}) = \frac{m_{\text{F}} C(t_{\text{ini}})}{\rho(t_{\text{ini}})}, \tag{4}$$

where m_{F} is the fuel consumption in units of kg per flight meter. We apply the dilution equation from Schumann et al. (1998) as follows:

$$C(t_{\text{ini}}) = 7,000 \left(\frac{t_{\text{ini}}}{t_0} \right)^{0.8}, \quad t_0 = 1 \text{ s}, \tag{5}$$

which is based on several in situ plume measurements at plume ages between 0.006 and 10^4 s. At given t_{ini}, A_{co} depends on the air density and the fuel consumption, which depends on the type of aircraft, its weight, speed, and thrust setting. The fuel consumption is calculated from the air traffic inventory (Section 2.4).

The ice crystal number per contrail length after the vortex phase is calculated as the product of $A_{\text{co}}(t_{\text{ini}})$ and $n_{\text{co}}(t_{\text{ini}})$, which is equivalent to the product of AEI_{ice} and m_{F}, is as follows:

$$N_{\text{ice}} = n_{\text{co}}(t_{\text{ini}}) \cdot A_{\text{co}}(t_{\text{ini}}) = \text{AEI}_{\text{ice}} \cdot m_{\text{F}}, \tag{6}$$

where the contrail length is the part of the flight distance that forms a contrail.

2.2. Present-Day Soot Particle Number Emissions

Soot particle number emissions from commercial aircraft during cruise vary greatly depending on aircraft engine type, plume age, fuel properties, and engine power settings and only few data from in situ measurement campaigns are available (e.g., Schumann & Heymsfield, 2017).

Anderson et al. (1998) investigated aircraft particle emissions over Virginia from the SNIF-II and over Kansas from the SUCCESS campaign. At cruise altitudes, they find EI_{s} to vary from $5 \cdot 10^{14}$ to $2 \cdot 10^{15}$ kg^{-1} for the more modern aircraft with high bypass engines and up to $5 \cdot 10^{15}$ kg^{-1} for older jetliners (Figure 1 of Anderson et al., 1998). Schumann et al. (2002) investigated within several SULFUR campaigns black carbon emissions around cruise altitudes behind different aircraft with known engine characteristics. While older aircraft reveal soot number emissions between $1.5 \cdot 10^{15}$ and $2 \cdot 10^{15}$ kg^{-1}, the more modern engines show significantly lower values of EI_{s} ranging between around $2 \cdot 10^{14}$ and $7 \cdot 10^{14}$ kg^{-1} (Figure 5 of Schumann et al., 2002). Petzold et al. (1999) performed measurements and estimated an average EI_{s} of $1.2 \cdot 10^{15}$ kg^{-1} for the aviation fleet of 1992.

Moore et al. (2017) obtained soot number emission indices between $2 \cdot 10^{14}$ kg^{-1} and $9 \cdot 10^{14}$ kg^{-1} in the exhaust of a DC-8 during the ACCESS campaign. An even more recent campaign measured soot number emission indices between $1.2 \cdot 10^{15}$ and $4.5 \cdot 10^{15}$ kg^{-1} with an average value of $2.5 \cdot 10^{15}$ kg^{-1} in the exhaust of an A320 (Bräuer et al., 2021a).

Based on these observations, we prescribe "present-day soot emissions" with a soot number emission index of $1.5 \cdot 10^{15}$ kg^{-1}, which we will use as the reference value in our global simulations (Section 2.3, Table 1). To analyze the uncertainty in initial contrail ice crystal numbers (Table 1b) and global mean RF due to contrail cirrus (Section 4.2.3), we define two different ranges of soot number emissions by setting EI$_s$ to $1 \cdot 10^{15}$ kg^{-1} ("low soot 1") and $2 \cdot 10^{15}$ kg^{-1} ("high soot 1") and to $5 \cdot 10^{14}$ ("low soot 2") and $3 \cdot 10^{15}$ kg^{-1} ("high soot 2"), according to the range of different observations.

2.3. Sensitivity of Ice Nucleation and Vortex Phase Survival

In an offline study, we investigate the number of formed ice crystals, the fraction of ice crystals surviving the vortex phase, and the ice crystal number after the vortex phase by applying the parameterizations described in Section 2.1.2 and 2.1.3. We systematically vary atmospheric temperatures and relative humidities with respect to ice typical for conditions at cruise altitude. We analyze our results for "present-day soot" (Section 2.2) and "reduced soot emissions" when decreasing present-day soot emissions by 80%. We assume a log-normal size distribution of soot particle with a geometric-mean dry core radius of 15 nm and a geometric width of 1.6, as deduced from observations in aircraft plumes at cruise altitudes (e.g., Moore et al., 2017; Petzold et al., 1999).

2.4. Climate Model Simulations and Model Setup

For our global simulations with ECHAM5-CCMod, we use the same setup as Bock and Burkhardt (2016a, 2019), a horizontal resolution of T42 that corresponds to $2.8° \times 2.8°$ in latitude and longitude on a Gaussian grid or about 300×300 km at the equator. The model grid is subdivided into 41 nonequidistant vertical hybrid pressure levels with an increased vertical resolution (about 500 m) near the tropopause (Kurz, 2007). The time step of the model is 15 min (see Figure 1). We prescribe the Atmospheric Model Intercomparison Project (AMIP II) sea surface temperature climatology (Taylor et al., 2000). We use the AEDT flight inventory describing air traffic for the year 2006 (Wilkerson et al., 2010) to obtain the flight distance and the fuel consumption. We prescribe a log-normal distribution for emitted soot particles as in the offline studies.

As in Bock and Burkhardt (2016a), we calculate the coverage due to contrail cirrus and natural clouds assuming maximum random (vertical) overlap and calculate the stratosphere adjusted RF (Stuber et al., 2001). The radiation scheme is called every hour twice, one time for natural clouds alone and one time for natural plus contrail cirrus cloudiness. This allows us to calculate contrail cirrus RF within one climate model simulation.

For the calculation of the ice crystal loss in the vortex phase, we derive for each grid box where persistent contrails form a range of relative humidity over ice from the subgrid-scale variability of the water vapor mass mixing ratio of the model's cloud scheme (Burkhardt et al., 2008). We subdivide this range into 5% humidity bins, apply the parameterization of Unterstrasser (2016) for each bin, and subsequently calculate the grid box average survival fraction.

To analyze the spatial variability in contrail ice crystal formation and ice crystal loss during the vortex phase, contrail cirrus properties and RF, we performed one simulation with present-day soot number emissions. Furthermore, we study the impact of reduced soot number emissions. As in the offline studies, we prescribe a considerable reduction in soot number emissions (by 80%), referring to it as the "reduced soot case" in order to obtain significant changes in the resulting contrail cirrus fields. We conduct two further simulations with a 50% and 90% soot number emission reduction to analyze the sensitivity of global mean contrail cirrus RF on aircraft soot particle emissions. These simulations have been run for 5 years. In order to study the uncertainty of our results due to the uncertainty and variability in present-day soot emissions (Section 2.2), we performed four additional simulations (two each with increased and decreased soot number emissions) each running for 3 years. Our analysis is given on pressure levels.

3. Sensitivity Studies for Ice Crystal Numbers After the Vortex Phase

In this section, we perform an offline study to investigate the ice nucleation in the jet phase and the ice crystal loss during the vortex phase and the interaction of these processes. We prescribe a constant air pressure of 240 hPa, typical for cruise altitudes. We vary ambient temperature (T_a) and relative humidity over ice (RH_i) and calculate contrail ice nucleation, ice crystal survival fraction, and the apparent ice number emission index after the vortex phase for the present-day case ($EI_s = 1.5 \cdot 10^{15} \, kg^{-1}$) and the reduced soot case ($EI_s = 3 \cdot 10^{14} \, kg^{-1}$). In the following, we introduce $\Delta T = |T_a - \theta_G|$ as the difference between T_a and the contrail formation threshold temperature θ_G, the latter defined in Section 2.1.1. Since θ_G depends on the ambient relative humidity over water, θ_G changes slightly for fixed RH_i and varying T_a.

Figure 2a depicts the apparent ice number emission index after nucleation (AEI_{nuc}, defined by Equation 1), as in Bier and Burkhardt (2019). Close to the contrail formation threshold ($\theta_G = 225.8 \, K$ for $RH_i = 120\%$ and $T_a = 225 \, K$), only few large soot particles can form ice crystals, resulting in low $AEI_{nuc} < 10^{13} \, kg^{-1}$. AEI_{nuc} steeply increases with decreasing temperature (and hence increasing ΔT) and then slowly approaches the soot number emission index of the respective emission scenario. Due to the low hygroscopicity of soot, we have adapted the parameterization of Kärcher et al. (2015) by improving the estimation of the critical saturation ratio for activating soot particles depending on the soot particle dry core radius (Appendix A). Therefore, our calculated AEI_{nuc} is close to the one of Bier and Burkhardt (2019) near the contrail formation threshold and shows larger deviations further away from the threshold approaching the soot number emission index (EI_s) faster. Relative differences in AEI_{nuc} to Bier and Burkhardt (2019) (not shown) are largest ($\approx 30\%$) at $\Delta T = 3 \, K$, slightly smaller ($\approx 20\%$) at $\Delta T = 2$ and 6 K, and around 10% at $\Delta T = 10 \, K$. Increasing RH_i to 140% and decreasing RH_i to 110% leads to a shift of the contrail formation threshold by around 0.5 and $-1.5 \, K$, respectively. As soon as the temperature threshold for contrail formation is well exceeded (by about 5 K), a variation in relative humidity has hardly any influence on contrail ice nucleation.

Figure 2b shows the fraction of ice crystals surviving the vortex phase (f_N), when setting AEI_{nuc} to EI_s, that is, when neglecting the impact of atmospheric parameters on ice nucleation. Generally, f_N continuously increases with decreasing temperature due to two reasons. On the one hand, the emitted engine water vapor causes a larger increase in ice-supersaturation in the aircraft wake at lower atmospheric temperature due to the nonlinear dependency of saturation vapor pressure on temperature. On the other hand, this nonlinear dependency also leads to a smaller decrease of relative humidity in the sinking vortices for lower temperatures and, therefore, to a lower sublimation loss. The survival fraction increases with rising ambient relative humidity. At 215 K, a typical temperature at cruise altitude, only around 9% of the nucleated ice crystals survive for present-day soot number emissions at slightly ice-supersaturated conditions ($RH_i = 110\%$, dotted blue line). f_N rises to 0.26 and 0.76 when RH_i is increased to 120% (thick solid blue) and 140% (dashed blue), respectively. These large f_N values are caused by an increasing number of ice crystals also surviving in the primary wake so that contrails frequently reach their full vertical extent at high ice-supersaturation (Unterstrasser, 2014). If fewer ice crystals form, for example, due to decreased soot number emissions, the available water vapor for deposition is distributed among fewer ice particles which in turn grow larger. Consequently, a smaller fraction of these ice crystals sublimate within the descending vortices. Therefore, f_N increases by a factor of around 2.3 when reducing AEI_{nuc} by 80% at $T_a = 215 \, K$ and $RH_i = 120\%$.

Allowing AEI_{nuc} to vary with atmospheric conditions (Figure 2c), f_N displays a minimum approximately at $\Delta T = 3 \, K$, which is more pronounced for lower ambient ice-supersaturation and increases strongly with rising T_a afterward. This increase of f_N results from the strong decrease of nucleated ice crystals when ambient temperature approaches the formation threshold (Figure 2a). Considering $RH_i = 120\%$, the minimum f_N is 0.19 for present-day and 0.43 for reduced soot number emissions.

To analyze the combined effect of ice nucleation in the jet phase and the sublimation loss in the vortex regime, we show in Figure 2d the apparent ice number emission index after the vortex phase (AEI_{ice}), as defined by Equation 2. For all RH_i, AEI_{ice} is close to EI_s at temperatures close to 200 K. For highly ice-supersaturated conditions ($RH_i = 140\%$), AEI_{ice} approaches the soot number emission index at T_a below 210 K as many soot particles can activate and subsequently freeze and many ice crystals can survive. Close to the contrail formation threshold ($\Delta T < 2 \, K$), AEI_{ice} is reduced due to the limited ice nucleation. At temperatures very lower than θ_G, where nearly all emitted soot particles can form ice crystals, AEI_{ice} is controlled by the ice crystal loss during the vortex
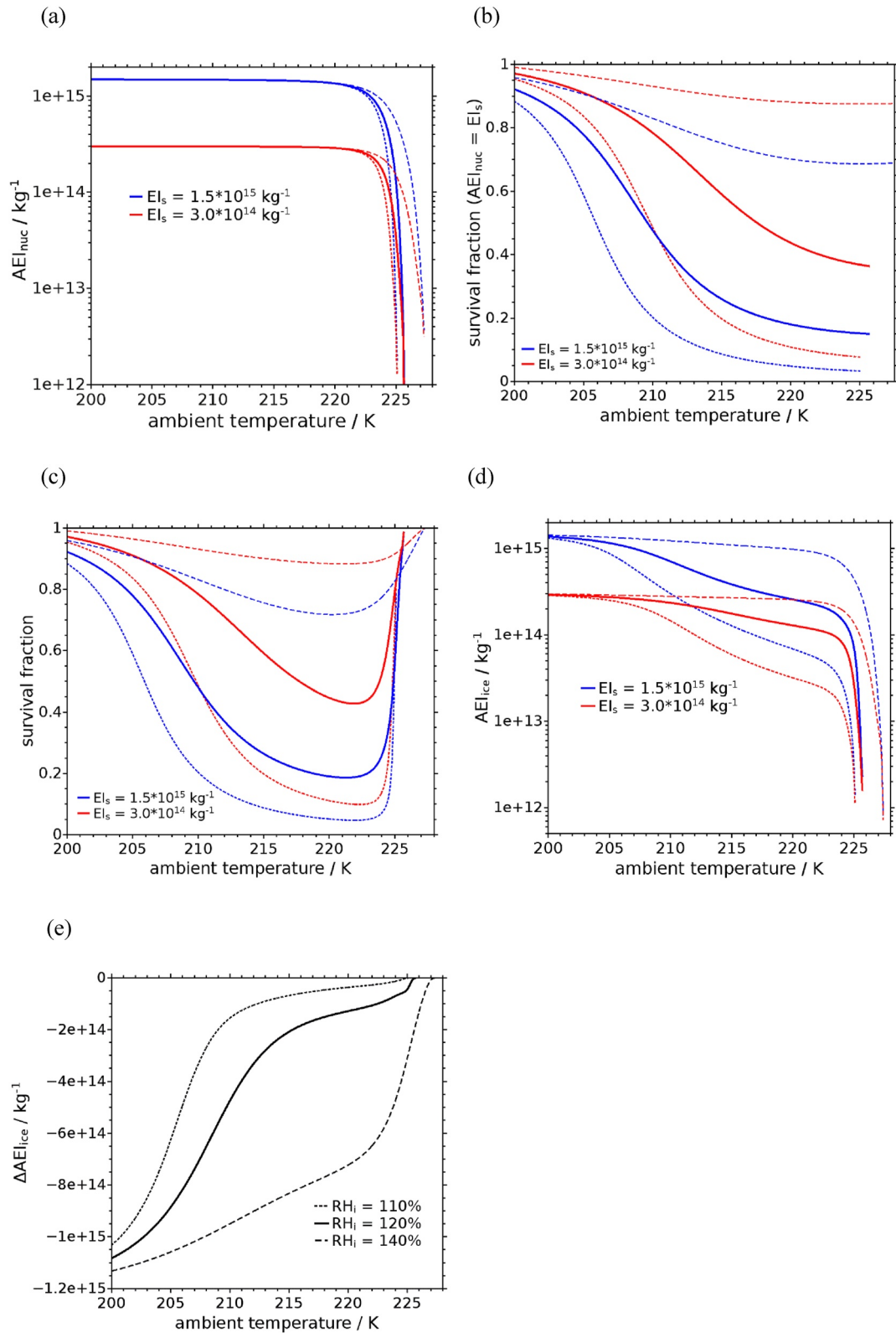
Figure 2.

phase. In a highly ice-supersaturated atmosphere (dashed lines in Figure 2d), AEI_{ice} behaves similar to AEI_{nuc} (Figure 2a) since more than around 70% (present-day soot case) or even more than 90% of ice crystals (reduced soot case) survive the vortex phase. Decreasing RH_i to 120% and 110%, the number of ice crystals after the vortex phase is clearly decreased compared to the nucleated ice crystal number (Figures 2a and 2d).

Figure 2e shows the absolute difference in contrail ice crystal number after the vortex phase (ΔAEI_{ice}) due to a decrease in soot number emissions by 80%. At a temperature of 200 K, $|\Delta AEI_{ice}|$ is largest (>10^{15} kg^{-1}) due to high nucleated ice crystal numbers and survival fractions (Figures 2a and 2b). While the difference in nucleated ice crystal numbers remains close to ΔEI_s (i.e., $1.2 \cdot 10^{15}$ kg^{-1}) at $\Delta T > 5$ K (Figure 2a), $|\Delta AEI_{ice}|$ decreases significantly with increasing temperature in the whole considered temperature range. This is because the ice crystal loss during the vortex phase counteracts the effect of reduced soot number emissions since fewer ice crystals sublimate during the vortex descent when ice nucleation is decreased (Unterstrasser, 2016). Consequently, $|\Delta AEI_{ice}|$ is significantly lower for the weakly (dotted line) than for the highly ice-supersaturated case (dashed line in Figure 2e). At temperatures between 215 and 220 K, AEI_{ice} is reduced only by around 50% for $RH_i = 110\%$ and by around 75% for $RH_i = 140\%$ due to the 80% soot emission reduction. At lower temperatures $|\Delta AEI_{ice}|$ is more strongly dependent on relative humidity than AEI_{ice}. $|\Delta AEI_{ice}|$ approaches zero near the contrail formation threshold due to the limited ice nucleation (Bier & Burkhardt, 2019).

4. Impact of Nucleation and Ice Crystal Loss on Properties of Young Contrails

Ice nucleation and ice crystal loss in the vortex phase strongly vary temporally and geographically leading to a large variability in the properties of young contrails. In Section 4.1, we present the spatial variability in contrail ice nucleation and the ice crystal loss during the vortex phase. We describe in Section 4.2 the resulting ice crystal numbers and contrail cross-sectional areas after the vortex phase at a contrail age of 450 s. We evaluate in Section 4.3 those ice crystal numbers of young contrails with in situ measurements accounting for the variability in present-day soot emissions.

4.1. Apparent Ice Number Emission Indices

Figure 3a shows the apparent ice number emission index after nucleation (AEI_{nuc}), defined by Equation 1, at 240 hPa (around the main cruise level). As discussed in Bier and Burkhardt (2019), in most areas of the northern extratropics contrails form frequently at temperatures much lower than the formation threshold so that AEI_{nuc} typically exceeds $1.35 \cdot 10^{15}$ kg^{-1}, that is, on average more than 90% of emitted soot particles form ice crystals. In the tropics, ice crystal formation on soot particles is limited by higher atmospheric temperatures and AEI_{nuc} ranges approximately between 10^{14} and $9 \cdot 10^{14}$ kg^{-1} so that AEI_{nuc} is on average around 40%–90% smaller than the soot number emission index. The lowest values of AEI_{nuc} occur over Indonesia and the Pacific Ocean as contrails often form very close to the formation threshold. Of the main air traffic areas, it is mainly the Southeastern USA and Eastern Asia where ice nucleation is significantly reduced.

Due to the modification of the parameterization of Kärcher et al. (2015) (see Appendix A), AEI_{nuc} is larger by 5%–10% in the northern extratropics, by around 10%–20% in the subtropics, and occasionally by more than 30% in some regions of the tropics compared to Bier and Burkhardt (2019). Note that these large percentage increases in the tropics are frequently connected with a low absolute difference in AEI_{nuc} due to the limited contrail ice nucleation near the formation threshold.

The fraction of ice crystals surviving the vortex phase (f_N) at 240 hPa, shown in Figure 3b, ranges between 0.4 and 0.55 in the northern extratropics with higher values over Asia due to lower ambient temperature. f_N tends to decrease toward the subtropics since atmospheric temperatures are increased. Lowest values of f_N (around 0.36) occur over Northern Africa and the subtropics over the Atlantic due to low mean ambient relative humidity. Despite increasing temperature, the survival fraction increases again toward the tropics and becomes even

Figure 2. Apparent ice number emission index (a) after nucleation (AEI_{nuc}) and (d) after the vortex phase (AEI_{ice}) with present-day (blue) and soot emissions reduced by 80% (red); fraction of ice crystals surviving the vortex phase for both soot emission scenarios when assuming (b) that all soot particles form ice crystals ($AEI_{nuc} = EI_s$) and (c) when ice nucleation is dependent on the atmospheric state and (e) absolute differences in AEI_{ice}, shown in (d), (low minus present-day soot) versus ambient temperature T_a. All quantities are shown for three different relative humidities over ice (RH_i, dotted line: 110%, thick solid line: 120%, dashed line: 140%) at an atmospheric pressure of 240 hPa. Note that for fixed RH_i the Schmidt-Appleman-threshold temperature θ_G slightly decreases with decreasing T_a. For $RH_i = 120\%$, θ_G equals 225.1, 225.5, and 225.8 K at T_a of 210, 220, and 225 K, respectively.
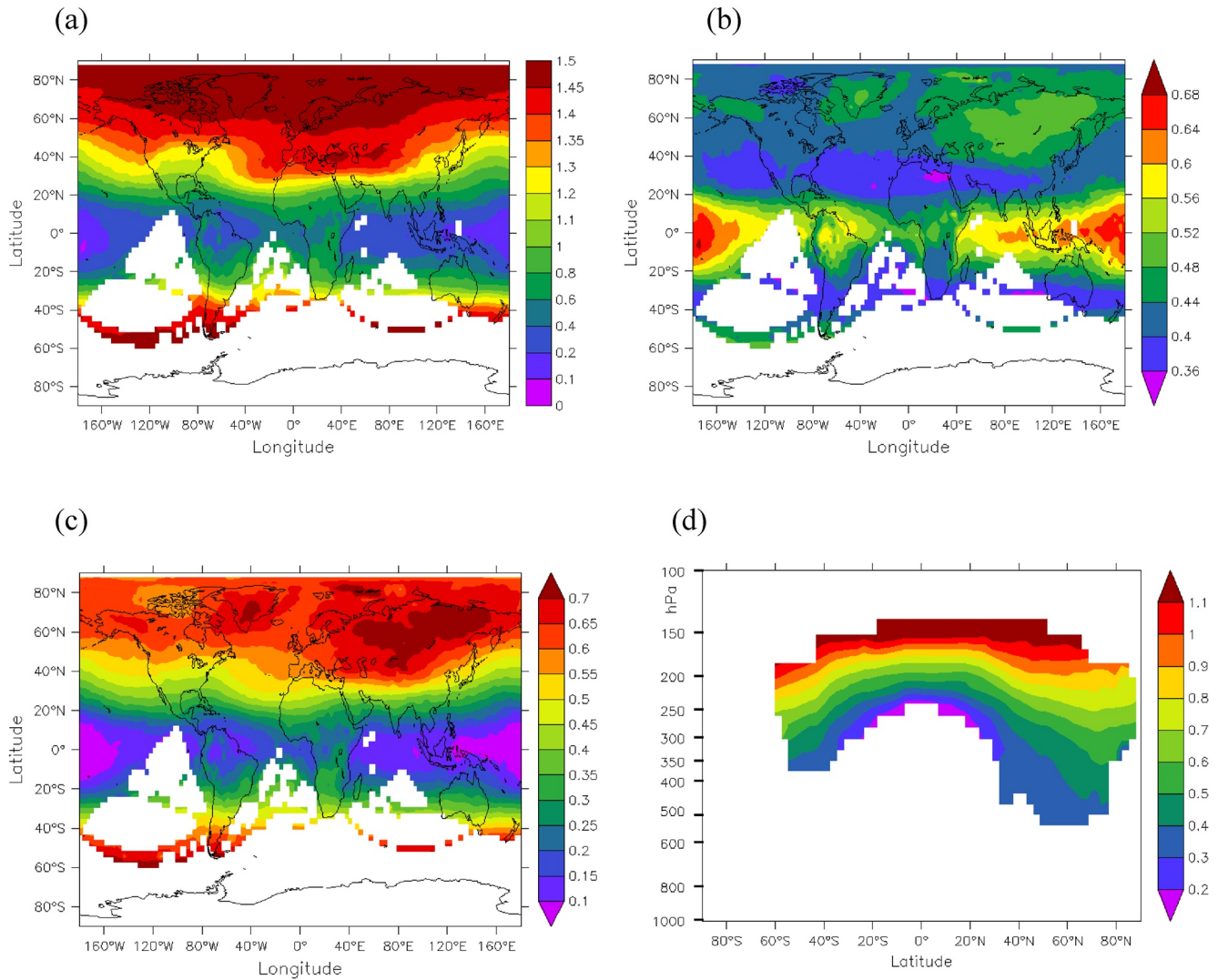
(a)

(b)

(c)

(d)

Figure 3. Global distribution of annual mean (a) apparent ice number emission index after nucleation in 10^{15} kg^{-1}, (b) fraction of ice crystals surviving the vortex phase, and (c) apparent ice number emission index after the vortex phase in 10^{15} kg^{-1} at 240 hPa. (d) Annual and zonal mean vertical profile of the apparent ice number emission index after the vortex phase in 10^{15} kg^{-1}. All displayed quantities are weighted with the newly formed contrail length and averaged only over incidents of contrail formation.

larger than in the extratropics. This is mainly due to the strong decrease in the number of nucleated ice crystals (Figure 3a) but also due to a higher mean relative humidity than in the subtropics. The largest survival fractions are seen over Indonesia and the Equatorial Pacific since AEI$_{nuc}$ is lowest in those regions.

Figure 3c shows the apparent ice number emission index after the vortex phase (AEI$_{ice}$) defined by Equation 4. The spatial global pattern of AEI$_{ice}$ is consistent with that of AEI$_{nuc}$. AEI$_{ice}$ is significantly decreased relative to AEI$_{nuc}$ in the northern extratropics and ranges between around $4 \cdot 10^{14}$ and $6 \cdot 10^{14}$ kg^{-1} in the USA and $5.5 \cdot 10^{14}$ and $7 \cdot 10^{14}$ kg^{-1} over central Europe. Even though the survival fraction is higher in the tropics than in the extratropics (Figure 3b), AEI$_{ice}$ is clearly lower in the tropics due to the limited contrail ice nucleation (Figure 3a).

Figure 3d depicts the zonal mean vertical profile of AEI$_{ice}$. In general, AEI$_{ice}$ decreases with decreasing altitude since ice nucleation is increasingly limited due to higher atmospheric temperature. The decline is strongest in the tropics where contrails form frequently close to the formation threshold even at cruise levels (Bier & Burkhardt, 2019). This decline is also significant in the extratropics where higher temperatures at lower altitudes lead to a larger ice crystal loss in the vortex phase (Figure 2c). The threshold altitude above which contrails are occasionally able to form is at the 400–500 hPa level in the extratropics and about the 300 hPa level in the tropics.
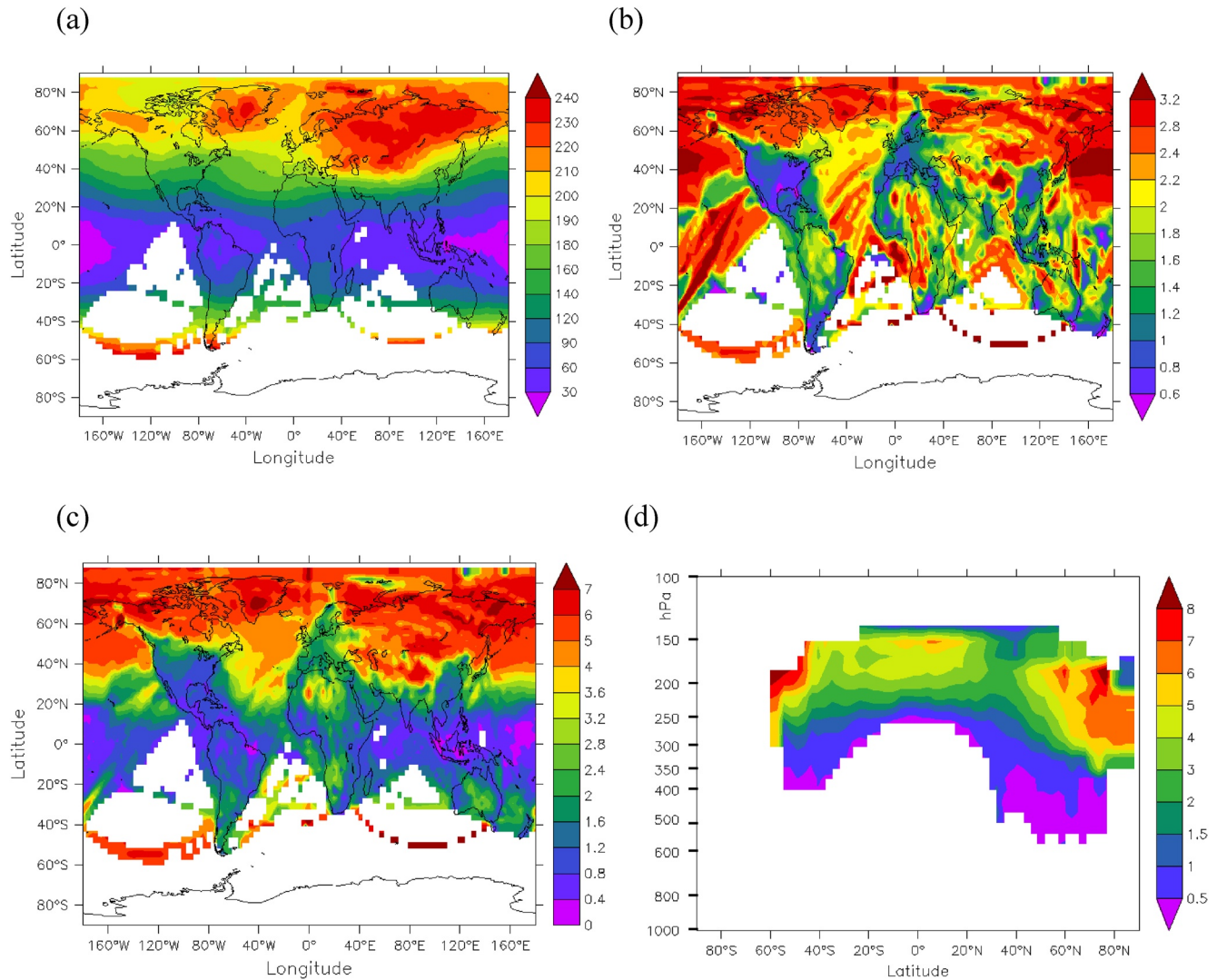
(a)

(b)

(c)

(d)

Figure 4. Global distribution of annual mean (a) in-cloud contrail ice crystal number concentration in cm^{-3}, (b) contrail cross-sectional area in 10^4 m^2, and (c) total number of ice crystals per contrail length (N_{ice}) in 10^{12} m^{-1} at 240 hPa. (d) Annual and zonal mean vertical profile of N_{ice} in 10^{12} m^{-1}. The quantities are shown for a contrail age of 450 s, the time of contrail initialization in the climate model. All displayed quantities are averaged only over incidents of contrail formation.

4.2. Ice Crystal Number Concentration and Contrail Cross-Sectional Area

In the following, we investigate the spatial distribution of contrail ice crystal number concentration (n_{co}), cross-sectional area (A_{co}), and ice crystal number per contrail length for young contrails ($N_{\text{ice}} = A_{\text{co}} \cdot n_{\text{co}}$) after the vortex phase (at an age of 450 s). First, we analyze global distributions at a cruise altitude at 240 hPa and, afterward we investigate zonal mean vertical profiles of these quantities.

Figure 4a shows the global distribution of the ice crystal number concentration. n_{co} ranges between 180 and 220 cm^{-3} over Europe, between 160 and 200 cm^{-3} over the North Atlantic, and between 120 and 180 cm^{-3} over the USA. The lower n_{co} over the USA and its decrease toward the south results from higher ambient temperatures and the accordingly decreased contrail ice nucleation (Figure 3a) and a larger ice crystal loss during the vortex phase (Figure 3b). n_{co} continuously decreases toward the tropics and falls below 60 cm^{-3} over Indonesia and the Indian/Equatorial Pacific since ice nucleation is strongly limited by ambient temperatures very close to the contrail formation threshold.

Figure 4b displays the global distribution of the average contrail cross-sectional area at 240 hPa. The variability in A_{co} at constant pressure results from the variability in fuel consumption and air density assuming a fixed

Table 1
Measured (a) and Simulated (b) Young Contrail Properties for Given Meteorological Conditions, Ambient Air Pressure (p_a), and Ambient Temperature (T_a)

Campaign	Contrail creating airplane and engine type	Age/s	p_a/hPa	T_a/K	n_{co}/cm^{-3}	A_{co}/10^4 m^2	m_F/10^{-3} kgm^{-1}	AEI$_{ice}$/10^{14} kg^{-1}	N_{ice}/10^{12} m^{-1}
(a)									
CONCERT	A319-111	112	241	217	162	–	2.4	4.5	1.08
	CFM56-5B6/P								
	A380-841	109		218	235	–	15.9	2.5	3.98
	Trent 970-84								
PAZI-2	Embraer-170	150	196	213	68.3	4.20	1.85	–	2.87
	Twin-engine	900		213	18.3	25.20	1.85	–	4.62
ECLIF II	A320 ATRA	134	206	206	–	–	2.06	11.5	2.37
	V2527-A5								

Model results		EI$_s$/10^{15} kg^{-1}	p_a/hPa	T_a/K	n_{co}/cm^{-3}	A_{co}/10^4 m^2	AEI$_{ice}$/10^{14} kg^{-1}	N_{ice}/10^{12} m^{-1}
(b)								
CoCiP estimate Schumann et al., 2017		**1**			40 (25%)	2.25 (25%)	–	0.9 (25%)
					100	**2.5**		**2.5**
					250 (75%)	2.8 (75%)		7.0 (75%)
ECHAM-CCMod		0.5 (low soot 2)	200	208	94	**1.64**	3.41 ± 0.71	1.53 ± 0.41
		1 (low soot 1)			169		6.15 ± 1.48	2.77 ± 0.81
		1.5 (reference)			**230**		**8.39 ± 2.19**	**3.77 ± 1.18**
		2 (high soot 1)			280		10.24 ± 2.88	4.59 ± 1.47
		3 (high soot 2)			405		14.87 ± 4.38	6.64 ± 2.24
Central Europe		0.5	240	211	90	**1.18**	2.80 ± 0.51	1.06 ± 0.24
		1			163		4.84 ± 1.01	1.92 ± 0.44
		1.5			**222**		**6.62 ± 1.51**	**2.62 ± 0.67**
		2			268		8.03 ± 1.70	3.16 ± 0.75
		3			350		10.97 ± 2.67	4.13 ± 1.17
ECHAM-CCMod zonal mean		0.5	240	211	90	**1.76**	2.73 ± 0.49	1.58 ± 0.37
		1			157		4.78 ± 0.97	2.76 ± 0.72
		1.5			**214**		**6.50 ± 1.37**	**3.77 ± 1.08**
Northern extratropics		2			261		8.00 ± 1.75	4.59 ± 1.35
		3			355		10.91 ± 2.59	6.24 ± 1.95

Note. For the observations in (a), the measurement campaign, the contrail creating aircraft with the engine type, and the estimated contrail age are given. For simulation results in (b), the model name, the soot number emission index and atmospheric parameters, the ambient air pressure (p_a), and ambient temperature (T_a) are given. Simulated contrail properties are shown at a contrail age of 450 s. For simulations and observations (if measured quantity is available), a consistent set of ice crystal number concentration (n_{co}), contrail cross-sectional area (A_{co}), apparent ice number emission index (AEI$_{ice}$), and ice crystal number per contrail length (N_{ice}) are given. For the observations, the displayed quantities are averages over several measured values during the contrail encounters. For ECHAM-CCMod, the results averaged over 5 years are given for five different soot number emission indices distinguishing between contrail properties averaged over central Europe both at 200 and 240 hPa and average values for the whole northern extratropics (40–70°N) weighted with contrail formation frequency at 240 hPa. Furthermore, the temporal standard deviations (from the 5 years) of the areal means are given for AEI$_{ice}$ and N_{ice}. Both the average values and the standard deviations comprise only incidents of contrail formation. For the CoCiP model, we give global average contrail properties and the 25th and 75th percentile (Figures 3 and 4 of Schumann et al., 2017). The bold values in (b) depict those contrail properties that either refer to our reference soot case or to the median of the CoCiP estimate.

plume dilution at the contrail age of 450 s (see Equation 4). Over Europe and the USA, fuel consumption (in units of kg per flight m) is relatively low since air traffic is dominated by smaller short-haul airplanes (Bier & Burkhardt, 2019). Consequently, A_{co} is relatively low (mostly $< 10^4$ m^2) over those areas whereas it is largest over the Pacific, where typically long-haul flights with larger aircrafts take place. Relatively high values ($A_{co} > 2 \cdot 10^4$ m^2) can also be found over the North Atlantic and certain regions over Asia and Africa.

The ice crystal number per contrail length (N_{ice}) (Figure 4c) ranges from around 1.8 to $3 \cdot 10^{12}$ m^{-1} over Europe. The zonal variability of N_{ice} mirrors the variability of the cross-sectional contrail area. N_{ice} over the USA is clearly lower ($<1.5 \cdot 10^{12}$ m^{-1}) than over Europe due to the lower contrail ice nucleation and survival fraction in the vortex phase. Additionally, over the Eastern USA N_{ice} is decreased due to very low values of A_{co} connected with a large number of short haul flights. In accordance with the contrail cross-sectional area, N_{ice} is relatively high over the North Atlantic and displays its maximum values ($>5 \cdot 10^{12}$ m^{-1}) over the North Pacific and certain regions of Canada and Asia.

Considering the zonal mean vertical profile of the ice crystal number per contrail length after the vortex phase (Figure 4d), N_{ice} typically exceeds $2 \cdot 10^{12}$ m^{-1} above the 200 hPa level due to large AEI$_{ice}$ at those altitudes (Figure 3d). Largest values ($>5 \cdot 10^{12}$ m^{-1}) occur in the northern high latitudes (between around 200 and 300 hPa) and result from the high fuel consumption connected with long distance flights of larger aircraft. Indeed, N_{ice} is quite low ($<10^{12}$ m^{-1}) below the 250 (300) hPa level in the tropics (subtropics) and below the 350 hPa level in the northern extratropics which is mainly due to the limited contrail ice nucleation at higher atmospheric temperatures.

4.3. Evaluation With Measurement Campaign Data

A large number of measurement campaigns have been conducted in the past years supplying us with data of contrail ice crystal number concentrations. The use of campaign data for model evaluation is difficult since not only measurements of the contrail properties and aircraft emissions but also contrail age and atmospheric state need to be known. Observed contrail ice crystal number concentrations (n_{co}) have been used in order to evaluate simulations (e.g., Bock & Burkhardt, 2016a). However, n_{co} varies directly with plume age and dilution hindering a suitable comparison between measurements and model results. While the apparent ice number emission index (AEI$_{ice}$) is independent of plume dilution, the ice crystal number per contrail length (N_{ice}) additionally contains information about the contrail cross-sectional area. Therefore, AEI$_{ice}$ and N_{ice} are better metrics for the comparison of young contrail properties with observational data. However, only few campaigns supplied associated estimates of these quantities in addition to the measurements of n_{co}. Here, we select three campaigns (performed over Germany) that comprise those estimates together with measured surrounding atmospheric data (temperature, pressure, and relative humidity over ice). We juxtapose the measurement data (Table 1a) and the simulated values averaged over central Europe (Table 1b) at 200 hPa for a comparison with the PArtikel und ZIrren (PAZI-2) campaign and the Emission and Climate Impact of Alternative Fuels (ECLIF II) campaign. Furthermore, we compare the simulated values averaged over central Europe at 240 hPa for a comparison with the Contrail and Cirrus Experiment (CONCERT).

Within CONCERT, Jessberger et al. (2013) and Schumann et al. (2013) investigated measurements of a few minutes old line-shaped contrails for different aircraft at. The Falcon probed the contrails at different positions with respect to the plume center. The observations have been performed under similar ambient conditions (ambient temperatures of 217–218 K and nearly ice-saturation) and at similar contrail ages (109–112 s), as displayed in Table 1. We calculate N_{ice} for each aircraft from the product of the measured apparent ice number emission index (AEI$_{ice}$) and fuel consumption (according to Equation 6). During the flight campaigns, AEI$_{ice}$ has been determined from the ratio of changing ice crystal number and NO$_y$ concentration at given NO$_x$ mass emission index (Schumann et al., 2013). For this method, the NO$_y$ concentration serves as a measure for the plume dilution assuming that NO and NO$_2$ are chemically inert in the first minutes of contrail formation. Here, we evaluate only AEI$_{ice}$ and N_{ice} (instead of n_{co}) to be independent of the different contrail age/plume dilution between the model and measurements.

We first compare our results (Table 1b, ECHAM central Europe at $p_a = 240$ hPa) with the measurements behind the A319 airplane keeping in mind that simulation results are for a mix of different aircraft with varying emission characteristics. Simulated AEI$_{ice}$ and N_{ice} in our reference run clearly exceed the measured values, but measured AEI$_{ice}$ still agrees well with our low soot 1 case and the measured N_{ice} with our low soot 2 case. One reason for the disagreement with the reference case is our on average higher fuel consumption (around $4 \cdot 10^{-3}$ kg m^{-1}) than recorded for the A319 ($2.4 \cdot 10^{-3}$ kg m^{-1}) causing larger simulated N_{ice}. On the other hand, the low observed AEI$_{ice}$ likely result from the atmospheric conditions that were close to ice-saturation leading to a high ice crystal loss during the vortex phase. Modeling results comprise several years of simulations averaging over situations characterized by varying degrees of ice supersaturation.

AEI_{ice} for the A380 is around half as large than for the A319 and even below our value of the low soot case 2. This low AEI_{ice} is likely caused by a higher ice crystal loss in the primary wake during the A380 measurements (Schumann et al., 2013) and, additionally, by lower soot number emissions per fuel mass of the more efficient A380 engine. In contrast, observed N_{ice} is significantly higher for the A380 than for the A319 since fuel consumption of the A380 is more than six times larger than for the A319 and 4 times larger than our average m_F over central Europe. Therefore, our simulated reference N_{ice} is 35% lower than measured but the observed N_{ice} agrees well with our high soot 2 case.

Within the PAZI-2 campaign, Febvre et al. (2009) measured a persistent contrail formed by an Embraer E170 over Berlin at 200 hPa, at 213 K, and a relative humidity over ice between around 110% and 130%. The contrail was probed at two time periods, first at about 150 s of age and later this contrail was encountered four times at ages between 660 and 1,200 s.

The Forward Scattering Spectrometer Probe (FSSP-300, 1–20 µm) has been used to determine the ice number densities n_{co}. Since no apparent ice number emission index was measured, we use the visually observed contrail width and height to obtain the contrail cross-sectional area (A_{co}) and to calculate N_{ice} as the product of n_{co} and A_{co}.

The comparison with our simulation results (Table 1b, ECHAM central Europe at $p_a = 200$ hPa) shows that the measured n_{co} are clearly lower while A_{co} are considerably larger. However, both quantities compensate each other so that our N_{ice} in the low soot 1 and high soot 1 simulations span the same range of values as indicated by observations. Simulated temperature is on average around 5 K lower than the measured temperature but since temperature lies well below the formation threshold the impact of this temperature difference is low. We find this to be an excellent agreement between simulated and observed N_{ice}.

Within the ECLIF II experiment, Bräuer et al. (2021b) measured contrails formed by an A320 over Northern Germany at 206 hPa and at plume ages between 93 and 143 s with a median value of 134 s. The in situ data comprise 400 contrail encounters with an over all measurement time of 2.5 hr. Although the aim of the campaign was to measure the effects of biofuel blends on contrail formation, we use measurements only from conventional kerosene for this evaluation. The measured average AEI_{ice} ($1.15 \cdot 10^{15}$ kg^{-1}) is by around a factor of 1.4 larger than our simulated reference AEI_{ice} (Table 1b, ECHAM central Europe at $p_a = 200$ hPa) but still matches our high soot uncertainty range. This is likely due to the relatively high soot number emissions of the A320 ATRA engines. Furthermore, the contrail measurements have been performed at high ambient ice-supersaturation with RH_i ranging between 122% and 141% and being on average 129%. This leads to a low ice crystal loss during the vortex phase and, therefore, higher AEI_{ice}. As for CONCERT, the observed N_{ice} is derived from the product of measured AEI_{ice} and m_F. The observed N_{ice} is even lower than our simulated reference N_{ice} and agrees well with our low soot 1 case. This is because m_F of the A320 is by slightly more than 50% lower than our simulated average m_F for central Europe.

Overall, our model results agree better with the PAZI-2 and ECLIF II observations due to moderately to highly ice-supersaturated surrounding conditions during the flights while the CONCERT ice crystal numbers tend to be lower owing likely to the low ambient relative humidity over ice time and possibly partly to lower soot number emissions. Averaging over the whole northern extratropics at the main cruise altitude (last rows in Table 1b), A_{co} is increased by around 50% compared to central Europe at 240 hPa. This is because the zonal mean average includes considerably higher A_{co} values over the North Atlantic and Pacific (displayed in Figure 4b) due to long-haul flights with higher fuel consumption. While A_{co} increases, n_{co} and AEI_{ice} stay very close to the European values. Consequently, N_{ice} averaged over the extratropics is increased relative to central Europe reaching values of $3.8 \cdot 10^{12}$ rather than $2.6 \cdot 10^{12}$ m^{-1} for the present-day soot case. This value agrees well with the observed average N_{ice} from the PAZI-2 campaign.

Finally, we compare our initial contrail ice crystal numbers with results from the Contrail Cirrus Prediction model (CoCiP), described in Schumann et al. (2015), that was applied to ECMWF data (Schumann et al., 2017). This model predicts contrail cirrus properties for given air traffic and weather prediction data. It simulates the life cycle of individual contrails behind a specific aircraft using a Lagrangian Gaussian plume model with simple bulk ice microphysics. CoCiP assumes that contrail ice nucleation is purely a function of soot number emissions. This is a relatively good estimate for upper tropospheric air traffic over Europe and the North Atlantic but unsatisfactory at the least for simulating contrail formation over the USA, Southeast Asia, generally the tropics (Figure 3a), and lower atmospheric levels (Figure 4f in Bier & Burkhardt, 2019). This leads in many cases to a

large overestimation of contrail ice crystal numbers. CoCiP further estimates the ice crystal loss during the vortex phase assuming that the surviving fraction is in line with the ice mass change (Schumann, 2012). This is a significant simplification since ice mass and ice crystal numbers evolve generally differently (Gierens & Bretl, 2009). Survival fractions within CoCiP are significantly higher than those inferred from LES likely leading to an overestimation in contrail ice crystal numbers.

We select CoCiP simulated contrail properties at a contrail age of around 450 s. We assume that most of the estimates from CoCiP come from air traffic at the main cruise level about 230 hPa. However, only a rough comparison with the CoCiP results can be performed since n_{co}, A_{co}, and N_{ice} are not given for specific regions at particular temperature, pressure, and relative humidity but rather averaged over all air traffic areas including different atmospheric conditions. In our comparison we primarily consider the "low soot 1" simulation as CoCiP uses a soot number emission index of 10^{15} kg^{-1}. Our simulated n_{co} over central Europe and the northern extratropics are higher than the CoCiP median value but still lower than the 75% percentile and our simulated A_{co} are generally smaller. While our calculated N_{ice} of $1.9 \cdot 10^{12}$ m^{-1} is lower over central Europe at 240 hPa, it is in good agreement with the CoCiP median of $2.5 \cdot 10^{12}$ m^{-1} over central Europe at 200 hPa and in the average over the northern extratropics at 240 hPa. This confirms our expectation that the averaging over the globe and to a smaller degree considering higher altitude levels leads to higher N_{ice} estimates. Moreover, the larger N_{ice} within the CoCiP model (in particular the 75% percentile estimate) may also hint at an overestimation of ice nucleation and a too low ice crystal loss during the vortex regime. On the other hand, our range of N_{ice} (1.5–$6.6 \cdot 10^{12}$ m^{-1}) resulting from the variability in soot number emissions ("low soot 2" to "high soot 2") lies well between the 25% and 75% percentile estimate from CoCiP indicating that the temporal and spatial variability of young contrail properties in both models are in reasonable agreement.

While N_{ice} varies with atmospheric conditions, soot number emissions, and fuel consumption in the present study, Bock and Burkhardt (2016b, 2016b, 2019) did not resolve the temporal and spatial variability in the initial conditions of young contrails. Guided by observations from measurement campaigns over Europe, they prescribed an initial ice crystal number concentration of 150 cm^{-3} and they fixed the initial contrail cross-sectional area at 450 s to $4 \cdot 10^4$ m^2 in line with the lidar measurements of contrails over Germany (Freudenthaler et al., 1995) resulting in $N_{ice} = 6 \cdot 10^{12}$ m^{-1} (Bock & Burkhardt, 2016b). This value lies within the range of N_{ice} simulated by ECHAM-CCMod with our improved setup but is very likely not a good average value for contrails over Europe or over the extratropics. Compared to our reference simulation the Bock and Burkhardt (2016a) initialization leads to N_{ice} values that are larger by about a factor of 2.3 over central Europe and the eastern USA at cruise altitude and on average by a factor of around 1.6 over the northern extratropics, suggesting a general overestimation of the total contrail ice crystal number. Even though the number of observational estimates used for this comparison is quite low and does not allow for a conclusive judgment, it is very likely that Bock and Burkhardt (2016a) overestimated N_{ice} significantly.

5. Impact of Variability in Young Contrail Properties on Contrail Cirrus

In the following, we present the mean global distribution of the microphysical and optical properties of contrail cirrus (averaged over all contrail ages and over 5 years) around the main cruise level at 240 hPa (Section 5.1) as well as the coverage of visible contrail cirrus and contrail cirrus RF (Section 5.2) for present-day soot number emissions. We analyze the impact of resolving the variability in contrail formation by comparing our results with Bock and Burkhardt (2016a), abbreviated with BB2016b hereafter. Finally, we discuss the uncertainty of our simulated contrail cirrus optical depth and RF in Section 5.3.

5.1. Contrail Cirrus Microphysical and Optical Properties

In this section, we investigate the global distribution of mean contrail cirrus ice crystal number concentration, ice water content, optical depth, and ice crystal volume radius. We expect for these quantities large differences compared to BB2016b in the tropics since BB2016b did not account for the dependence of contrail ice nucleation on the atmospheric state and instead prescribed constant ice crystal numbers for young contrails based on measurements over central Europe (Section 4.3).

Over nearly all of the extratropical main air traffic areas (north of about 30° latitude), high contrail cirrus ice crystal number concentrations (n_{cc}) above 20 cm^{-3} can be found (Figure 5a). Maximum n_{cc} (40–50 cm^{-3}) are
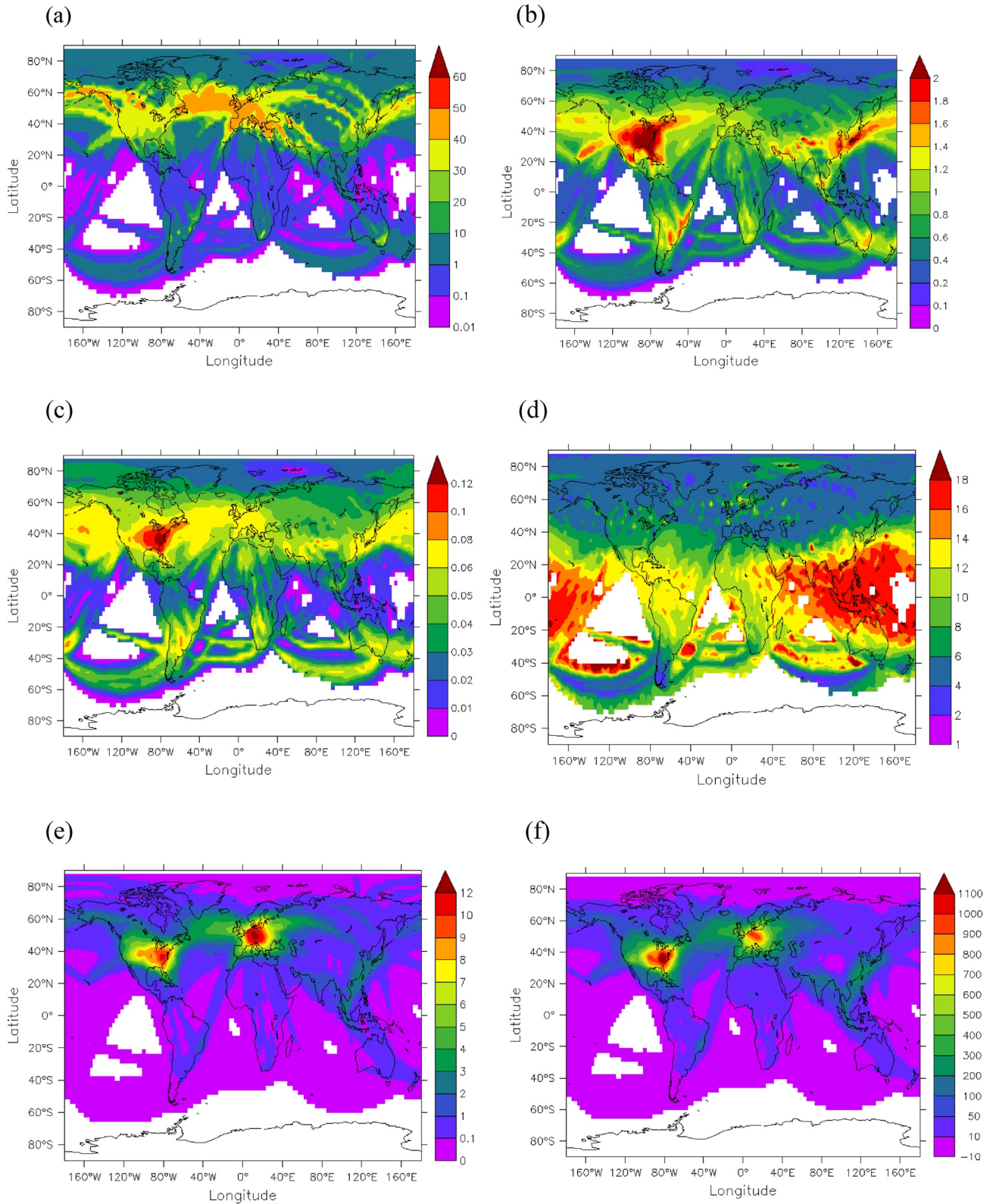
(a)

(b)

(c)

(d)

(e)

(f)

Figure 5.

situated within the main air traffic areas over Europe, the North Atlantic, and locally in the main flight tracks over the North Pacific and over Asia, Canada, and Alaska. These high n_{cc} are consistent with the fact that those areas are located in areas with high contrail formation frequency so that concentrations are significantly influenced by the properties of young contrails. Over the USA ice nucleation is decreased relative to the other main air traffic areas, which leads to a significantly lower ice crystal number concentration over the USA (20–40 cm^{-3}) than, for example, over Europe. While n_{cc} are comparable over central Europe and slightly higher over the North Atlantic than in BB2016b, they are lower over the eastern USA (Figure 6a). Our n_{cc} in the tropical regions are even by at least one order of magnitude lower than in BB2016b. Lower n_{cc} lead on average to shorter contrail cirrus lifetimes and a decrease in the contrail lifetime-integrated ice water content (Bier et al., 2017).

The global distribution of ice water content (Figure 5b) resembles the water vapor mass available for deposition (not shown). Mean ice water content tends to be large in air traffic areas where specific humidity is large and contrails form at temperatures much lower than the contrail formation threshold. Mean ice water content is largest (>2 mg m^{-3}) over the eastern USA and Japan. High values (1–2 mg m^{-3}) are also reached over Europe, Southern Asia, the North and South Pacific, South America, and Eastern Australia. Ice water content over Northern Asia is significantly lower due to colder and drier atmospheric conditions. The contrail cirrus ice water content is similar to the estimate of BB2016b over the North Atlantic, Northern Asia, and eastern USA. Our values are larger over Europe and the western USA but statistically not significant (hatched pattern in Figure 6b). Our mean contrail cirrus ice water content is by 70%–90% lower over Indonesia and the Equatorial Pacific and at least by 50% lower in other tropical regions than in BB2016b.

The contrail cirrus volume radius is diagnosed from contrail cirrus ice number concentration and the ice water content. Average volume radii of contrail cirrus ice crystals (Figure 5d) typically range between around 4 and 8 μm over the northern extratropics with slightly larger values (up to 10 μm) over the USA and Northern Europe. The average volume radii over the tropics frequently exceed 12 μm with maximum values of around 16 μm over the Pacific and Indian Oceans and Indonesia. Simulated ice crystal volume radii agree relatively well with the results of BB2016b over Northern Asia and the Atlantic, but are significantly increased (by more than a factor of 2) over the USA, central Europe, Southeast Asia, and Indonesia (Figure 6d).

In the following, we analyze the contrail cirrus optical depth that assumes a minimum ice crystal radius of 10 μm since this is the ice crystal radius threshold of the climate model radiation scheme (BB2016b). The average optical depth (Figure 5c) is relatively high (above 0.06) over the main air traffic areas of Europe and the USA and in the North Atlantic and North Pacific flight corridors and very small over the tropics (mostly below 0.05). The peak values (>0.1) are located over the eastern USA. The average optical depth over the USA significantly exceeds the values over Europe and within the North Atlantic and North Pacific routes. This is because the ice water content over the USA is larger than over Europe and overcompensates the impact of the lower ice crystal number concentration on optical depth. Figure 6c shows that the optical depth over the extratropics agrees well with the results by BB2016b. In contrast, optical depth is substantially decreased in the tropical and subtropical areas, in particular over Southeast Asia and the Southern USA and Mexico. However, the impact of the strongly decreased optical depth on global RF is limited due to the relatively low air traffic density and contrail formation probability in the tropics.

Finally, our results indicate that the global distribution of contrail cirrus ice crystal number concentration, ice water content, and optical depth (Figures 5a–5c) agree reasonably well with the results of BB2016b in the extratropics, whereas the differences in the tropics are very large for all quantities.

5.2. Contrail Cirrus Coverage and Radiative Forcing

In the following, we investigate the mean coverage due to all contrail cirrus with an optical thickness of at least 0.05 as this was estimated to be the optical thickness threshold for contrail cirrus to be detected with passive remote sensing methods (Kärcher et al., 2009). This mean coverage is not the coverage that would be visible

Figure 5. Global distribution of contrail cirrus (all ages) (a) in-cloud ice crystal number concentration in cm^{-3}, (b) in-cloud ice water content in mg m^{-3}, (c) optical depth, and (d) volume radius in μm at 240 hPa; the global distribution of (e) contrail cirrus coverage connected with an optical thickness of at least 0.05 in percent and (f) of the net radiative forcing due to contrail cirrus in mWm^{-2} is shown. The displayed quantities in (a)–(d) are averaged only over incidents where contrail cirrus occur. Note that the optical depth used for limiting the coverage in (e) is not the one shown in (c) but is instead diagnosed from contrail cirrus ice water path and ice crystal number concentration without introducing a minimum ice crystal radius (Bock & Burkhardt, 2016a).
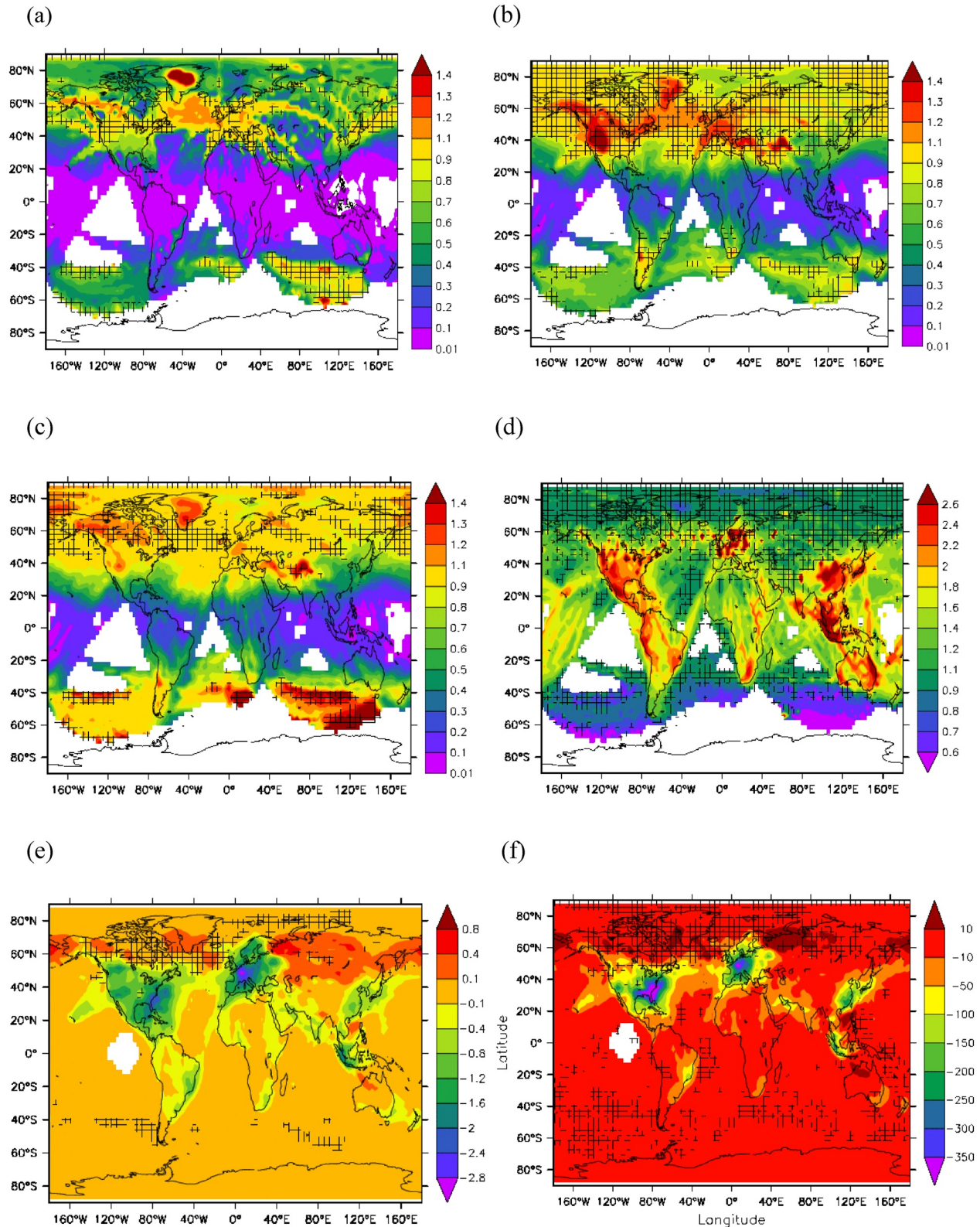
Figure 6. Comparison of the results shown in Figure 5 with the results of Bock and Burkhardt (2016a) (BB2016b): Global distribution of the ratio (present study/BB2016b) of contrail cirrus (all ages) (a) in-cloud ice crystal number concentration, (b) in-cloud ice water content, (c) optical depth and, (d) volume radius at 240 hPa and absolute differences (present study minus BB2016b) in (e) contrail cirrus coverage with optical thickness of at least 0.05 in % and (f) net radiative forcing by contrail cirrus in mWm^{-2}. The hatched pattern shows the regions where the differences are statistically not significant at the 99% level.

from the earth surface or from a satellite since many of those contrail cirrus will be hidden by natural cloudiness. Instead, we show the coverage that results from a vertical overlap of all contrail cirrus irrespective of whether they would be visible or not. The global mean coverage due to all contrail cirrus is 1.2%, just as in BB2016b, and when considering contrail cirrus with an optical thickness of at least 0.05 only 0.60%, about 20% smaller than in BB2016b. Figure 5e shows that $C_{0.05}$ is largest over the northern extratropical main air traffic areas with peak values (>10%) over central Europe and the eastern USA. Consistent with BB2016b, $C_{0.05}$ over central Europe tends to be higher than over the USA because a high fraction of contrail cirrus is transported from the North Atlantic toward Europe. $C_{0.05}$ is between 2% and 3% over some areas of Southeast Asia and does not exceed 1% in the majority of the remaining air traffic regions. Considering the vertical overlap of natural and contrail cirrus, the visible increase in cloudiness can be calculated by multiplying the contrail cirrus coverage (Figure 5e) by the fraction of contrail cirrus coverage leading to an increase in the overlapped cloud coverage (see Bock & Burkhardt, 2016a, Figure 6b). The fraction of contrail cirrus coverage leading to an increase in the overlapped cloud coverage is about 40% over Europe and about 50% over the USA. Additionally, the patterns of cloud cover increase differ significantly from those of the contrail cirrus cover. Finally, of the contrail cirrus that lead to an increase in cloudiness only a small part will be recognizable as contrail cirrus since aged contrails may not exhibit the typical line shape any longer.

The global mean longwave and shortwave RF due to contrail cirrus amount to 84.7 and −41.1 mWm⁻², respectively. This leads to a net RF of 43.6 mWm⁻². The compensation between shortwave and longwave forcing is 48.5%. The uncertainty range of the net RF is 42.3 and 45.6 mWm⁻² based on the global and annual mean RFs of the single years. The low interannual variability of global mean contrail cirrus RF is likely caused by the use of a sea surface temperature climatology. The fixed flight inventory additionally leads to a low variability in contrail cloud top height and, therefore, longwave contrail RF. Similar to the global distribution of $C_{0.05}$, the net RF is largest over the main air traffic areas and reaches maximum values (>800 mWm⁻²) over the eastern USA and central Europe. The annual mean net RF ranges between 100 and 300 mWm⁻² over Southern Asia and does not exceed 100 mWm⁻² over the remaining air traffic regions (Figure 5f).

Consistent with our lower values of N_{ice} compared to BB2016b (Section 4.3), the coverage due to contrail cirrus that has an optical thickness larger than 0.05 is significantly decreased in our study over Europe and the USA but also over Southeastern Asia and Indonesia (Figure 6e). The largest decrease occurs downwind of the main air traffic areas, that is, by around 1–2 percentage points (pp) over the East coast of the USA and by around 2–3 pp over central Europe indicating shorter contrail cirrus lifetimes. Consequently, the net RF over central Europe and the Southeastern USA is significantly lower in our study compared to BB2016b (Figure 6f). Our calculated global mean RF is 22% lower than in BB2016b for the year 2006. We find that this decrease is in particular due both to the smaller N_{ice} in the extratropical main air traffic areas and to the limited contrail ice nucleation in the tropics and subtropics.

5.3. Uncertainty in the Optical Depth and Radiative Forcing Estimate

Radiation parameterizations within global climate models are usually valid only for larger particles that exceed a certain threshold radius of about 10 μm (Roeckner et al., 2003). This is because the wavelength of light scattering can be determined based on geometric optics for the larger particles (Hansen & Travis, 1974), whereas for smaller particles Mie scattering needs to be considered. Estimating contrail cirrus optical depth while limiting ice crystal radii to values above 10 μm introduces an uncertainty in the optical depth values (BB2016b). When decreasing the minimum ice crystal radius while keeping ice water content fixed, contrail cirrus optical depth increases (Figure A2 in BB2016b). This increase is particularly large in regions where the ice water content is relatively high and ice crystal radii are low (BB2016b), that is, over the North Atlantic, Europe, and Northern Asia (Figures 5b and 5d). BB2016b find that the global mean contrail cirrus RF changes only by about 5% when decreasing the threshold radius from 10 to 6 μm in their simulations. Because our simulated radii are on average larger than in BB2016b due to reduced ice nucleation and since mean ice crystal radii reach values of around 10 μm over the USA and Japan, the uncertainty connected with our contrail cirrus RF estimate is lower than in BB2016b.
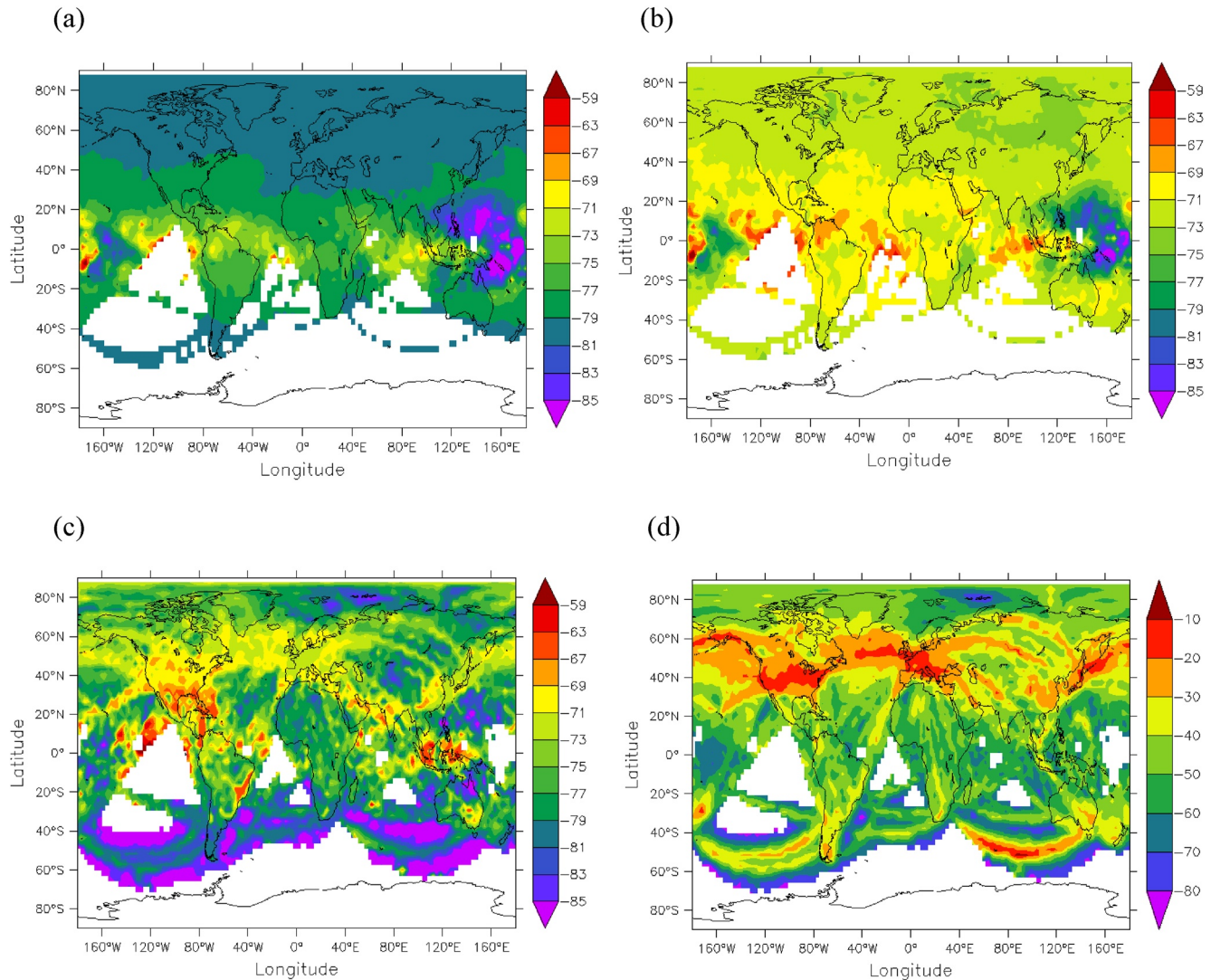
(a)

(b)

(c)

(d)

Figure 7. Global distribution of percentage change of apparent ice number emission index (a) after nucleation and (b) after the vortex phase and percentage change of contrail cirrus (all ages) in-cloud (c) ice crystal number concentration and (d) ice water content due to an 80% reduction of present-day soot number emissions at 240 hPa. The displayed changes are calculated from the quantities averaged only over incidents of contrail formation and are statistically significant within the 99% level.

6. Influence of Reduced Soot Number Emissions

Here, we investigate the impact of 80% reduced soot number emissions on the global distribution in contrail ice nucleation, ice crystal loss within the vortex phase (Section 6.1), contrail cirrus microphysical properties at 240 hPa (Section 6.2), as well as on contrail cirrus coverage and the RF (Section 6.3). Our objective is to evaluate the impact of including the parameterizations for contrail ice nucleation and ice crystal loss in the vortex phase on the sensitivity of contrail cirrus properties on initial ice crystal numbers or soot number emissions by comparing our results with Burkhardt et al. (2018). Furthermore, we study the sensitivity of the global mean contrail cirrus RF on different soot number emissions.

6.1. Change in Ice Nucleation and Vortex Phase Loss

As in Bier and Burkhardt (2019), the change in the number of nucleated ice crystals (AEI$_{nuc}$) due to reduced soot number emissions is nearly equal to the change in the soot emissions in the extratropical regions (Figure 7a). The decrease of AEI$_{nuc}$ is slightly lower over the USA due to higher ambient temperatures. In the tropics, the change

of AEI_{nuc} is frequently below 75% with lowest reductions over Western Indonesia and the Indian Ocean. This is because contrail formation in those areas often occurs close to the contrail formation threshold and, therefore, for reduced soot number emissions, a larger fraction of soot particles can activate into water droplets. Furthermore, the activation of the more hygroscopic ambient aerosol particles entrained into the plume becomes more relevant and weakens the effect of soot number emission reductions. In particular in areas with low air traffic volume, the nonlinear dependency of ice nucleation on atmospheric conditions and the averaging over a low number of contrail formation cases can lead to fluctuations in the percentage reductions and values of above 80% (Figure 4a). Compared to the results of Bier and Burkhardt (2019), we find that our correction of the critical saturation ratio for the activation of soot particles (Appendix A) leads to a slight increase in the change of AEI_{nuc} over the extratropics, resulting in a change closer to the soot number emission reduction.

The number of ice crystals after the vortex phase (Figure 7b) is decreased by only around 70%–72% in the extratropics since the ice crystal loss during the vortex phase counteracts the effect of decreased nucleated ice crystal number (resulting from reduced soot number emissions). This is because a lower fraction of the larger ice crystals sublimate within the descending vortices as described in Section 3. In the tropics, where contrails form quite close to their formation threshold, the decrease in AEI_{ice} is occasionally below 70% and hence significantly lower than the decrease in soot number emissions (Figure 7a).

6.2. Impact on Contrail Cirrus Microphysical Properties

The reduction of n_{cc} in the main air traffic areas over USA, Europe, North Atlantic, and the northern Pacific is around 70% (Figure 7c), relatively close to the reduction of EI_s, since in those areas contrail cirrus properties are strongly influenced by young contrails. In areas with lower air traffic density this reduction tends to be around 80%. Lower ice crystal numbers in the young contrails are associated with larger ice crystal sizes and enhanced sedimentation. As the differences in the sedimentation loss of contrails associated with different soot number emissions increase initially with lifetime (Bier et al., 2017), the decrease in n_{cc} in areas with low air traffic density and, therefore, with a higher fraction of aged contrails, tends to be higher than over the main air traffic regions.

Generally, contrail cirrus ice water content is reduced due to reduced soot number emissions. In most of the main air traffic areas this reduction in ice water content (iwc_{cc}, Figure 7d) is below 40%. Minimum reductions of iwc_{cc} (10%–20%) occur in areas of largest air traffic density over Europe, the USA, and the Atlantic and Pacific flight corridor. Those minima in the reduction frequently coincide with the minima in the reduction of ice crystal numbers. Since n_{cc} remains large in those areas even at reduced soot emissions, depositional growth of ice crystals is, just as in young contrails, mainly controlled by the availability of water vapor (Bier et al., 2017). Our simulated reduction in iwc_{cc} in the main air traffic areas of the extratropics is slightly lower than in Burkhardt et al. (2018). This is because that study assumes that an 80% reduction in soot number emissions leads to an 80% reduction in ice crystal numbers while we find that this reduction is smaller mainly due to the ice crystal loss during the vortex phase (Section 6.1). In most of the regions where flight density is low and the majority of contrail cirrus consists of aged contrails, the reduction in iwc_{cc} is clearly higher than in the main air traffic areas. This is because the low ice crystal number concentration of aged contrail cirrus limits the growth of contrail ice mass due to deposition of water vapor (Bock & Burkhardt, 2016b). Furthermore, the low ice crystal numbers allow for a faster ice crystal growth which can then lead to enhanced sedimentation, further reducing ice crystal number concentrations (Bier et al., 2017).

The global distribution of contrail cirrus optical depth (not shown) changes qualitatively similar to that of ice water content when reducing soot number emissions.

At 240 hPa, the global mean contrail cirrus ice number concentration weighted with contrail cirrus coverage is around 22.6 cm^{-3} and global mean ice water content amounts to around 1.1 mg m^{-3} for present-day soot emissions and the global mean optical depth is 0.055. The global mean reduction of n_{cc}, iwc_{cc}, and optical depth is about 71%, 29%, and 48% for a reduction in soot number emissions by 80%, respectively.

6.3. Decrease in Coverage and Radiative Forcing by Contrail Cirrus

While the global mean coverage of all contrail cirrus remains at around 1.2%, the global mean coverage of contrail cirrus with optical thickness larger than 0.05 ($C_{0.05}$) decreases from 0.60% to 0.25% when decreasing
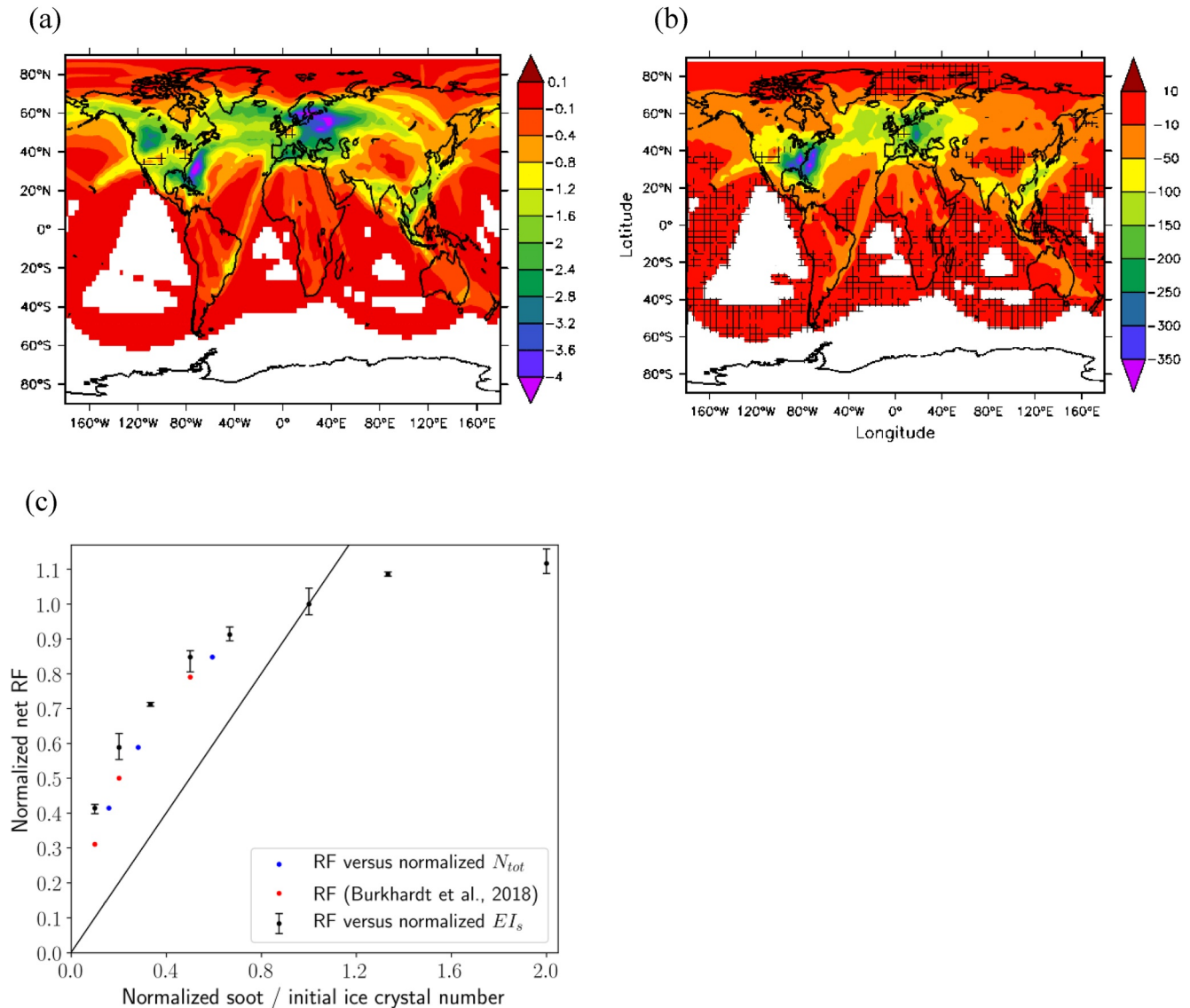
Figure 8. Global distribution of absolute differences in (a) contrail cirrus coverage with optical thickness of at least 0.05 in % and (b) net radiative forcing by contrail cirrus in mWm^{-2} between 80% reduced soot and present-day soot number emissions (reduced soot minus present-day soot), the hatched pattern show the regions where the differences are statistically *not* significant at the 99% level. (c) Depicts the global mean normalized net radiative forcing by contrail cirrus depending on normalized soot number emission index (EI$_s$, black circles) with the bars indicating the full range of single year mean radiative forcings, and on the normalized globally summed total ice crystal number after the vortex phase (N_{tot}, blue circles). Furthermore, the mean net radiative forcing depending on the normalized initial contrail ice crystal number as calculated by Burkhardt et al. (2018) (red circles) is shown.

soot number emissions by 80%. The largest absolute differences in $C_{0.05}$ (>3 pp, Figure 8a) occur downwind of the areas with maximum coverage (Figure 5e) and air traffic. This is because the fraction of aged contrail cirrus is large in those areas. Reducing soot number emissions frequently leads to a shortening of the contrail cirrus lifetime due to faster growth of the ice crystals and enhanced sedimentation loss (Bier et al., 2017) and to a drop in the optical thickness of aged contrails below the optical thickness threshold. In the tropical regions, it is mainly Southeast Asia where the absolute decrease in $C_{0.05}$ (>1 pp) is high.

The absolute decrease in contrail cirrus RF (Figure 8b) is highest (<−250 mWm^{-2}) downwind of the air traffic maximum over the eastern USA. Large reductions (<−100 mWm^{-2}) also occur over the North Atlantic and eastern Europe. Differences in RF over western Europe and the Northwestern USA tend to be smaller. Consistent with the change of $C_{0.05}$, largest reductions of the RF in the tropics (<−50 mWm^{-2}) occur over Southeast Asia and Western Indonesia.

Table 2
Global Mean Short Wave (RF_{SW}), Longwave (RF_{LW}), and Net Radiative Forcing (RF) due to Contrail Cirrus for the Different Simulations Varying With the Soot Number Emission Index (EI_s) Averaged Over Five Simulated Years for the Present-Day (Bold) and Reduced Soot Cases (Green Color) and Over Three Simulated Years for the Remaining Soot Uncertainty Cases

Simulation name	$EI_s/10^{15}$ kg^{-1}	$RF_{SW}/$ mWm^{-2}	$RF_{LW}/$ mWm^{-2}	RF/mWm^{-2}
90% reduction	0.15	−15.07	33.16	18.09 (17.36, 18.55)
80% reduction	0.30	−22.03	47.71	25.68 (24.17, 27.42)
Low soot 2	0.50	−27.36	58.43	31.07 (30.81, 31.10)
50% reduction	0.75	−33.57	70.56	36.99 (35.13, 37.79)
Low soot 1	1.00	−36.36	76.18	39.82 (39.04, 40.77)
Reference	**1.50**	**−41.05**	**84.70**	**43.65 (42.29, 45.61)**
High soot 1	2.00	−45.13	92.50	47.37 (47.12, 47.65)
High soot 2	3.00	−46.97	95.69	48.72 (47.46, 50.52)

Note. The values in parentheses display the full range of the single year averaged RFs.

We investigate the sensitivity of global mean RF on soot number emissions. In addition to our 80% soot number reduction simulation and the simulations connected with low and high soot numbers defining the uncertainty range of soot number emissions as defined in Section 2.2, we also perform simulations for a 50% and a 90% reduction in soot number emissions as in Burkhardt et al. (2018). While Table 2 summarizes the absolute global mean RF values, Figure 8c displays the relative change of global mean RF (black circles) with respect to our present-day soot case. It is clearly visible that the global RF depends nonlinearly on the soot emission reductions. The ice crystal loss within the vortex phase partially counteracts the decrease in the nucleated ice crystal number so that our global RF decreases more weakly with decreasing EI_s than in the study of Burkhardt et al. (2018) (red circles). Therefore, we also show the relative reduction of global RF with the normalized total nucleated ice crystal number surviving the vortex phase (N_{tot}) (blue circles). Reductions of our present-day soot emission scenario by 50%, 80%, and 90% lead to reductions in N_{tot} by around 41%, 72%, and 84% and cause the global RF to decrease by around 15%, 41%, and 59%, respectively. The decrease in global RF with N_{tot} is in good agreement with Burkhardt et al. (2018).

For the simulations connected with our uncertainty range, the global RF decreases by around 9% and 29% for 33% and 66% present-day soot emission reduction and increases by around 8.4% and 11.5% for both an increase in present-day soot emission by 33% and 100%, respectively (black circles). The slight increase in global RF for the high soot case 2 emphasizes the nonlinearity between contrail cirrus RF and soot number emissions.

7. Conclusions

Initial contrail properties can have a strong impact on the further development of contrail cirrus and their properties and lifetime (e.g., Bier et al., 2017; Burkhardt et al., 2018; Unterstrasser & Gierens, 2010). Recent studies have investigated properties and RF due to contrail cirrus using idealized assumptions for initial contrail ice crystal numbers. Bock and Burkhardt (2016a, 2019) assume initial contrail ice crystal numbers in line with observations over Europe and Chen and Gettelman (2013) calculate initial ice crystal numbers as a function of the available water vapor for deposition assuming a fixed ice crystal size typical for young contrails. Schumann et al. (2015) assume that every emitted soot particle forms an ice crystal and estimate the ice crystal loss within the vortex phase from the loss of ice water. To improve the initialization of contrails, we include a parameterization for contrail ice nucleation (Kärcher et al., 2015) and ice crystal loss during the contrail vortex phase (Unterstrasser, 2016) within the contrail cirrus scheme of ECHAM5 in the present study. The spatial variability in contrail ice nucleation has been investigated in more detail in Bier and Burkhardt (2019). Here, we focus on the combined variability of ice nucleation and ice crystal loss in the vortex phase and on the impact of parameterizing both processes for contrail cirrus properties and RF.

We show that the apparent ice number emission index is close to the respective soot number emission index for very low ambient temperatures and highly ice-supersaturated conditions. For moderate ice-supersaturation, the ice crystal loss within the vortex phase leads to lower initial ice crystal numbers even at temperatures of 15–20 K below the contrail formation threshold temperature. At temperatures close to the formation threshold, initial ice crystal numbers drop strongly due to decreases in ice nucleation while more ice crystals survive the vortex phase due to larger ice crystal sizes.

While in the northern extratropics ice nucleation is high due to air traffic occurring mostly at temperatures much lower than the contrail formation threshold, the common occurrence of moderate ice supersaturation typically leads to reduced ice crystal numbers due to significant losses in the vortex phase. In the tropics, the ice crystal number after the vortex phase is mainly determined by the limited ice nucleation due to atmospheric temperatures near the contrail formation threshold (Bier & Burkhardt, 2019). In most of the areas with high air traffic density, it is the variability in ice crystal loss that controls the initial contrail properties except for the Southeastern USA where higher ambient temperatures limit contrail ice nucleation. Including parametrizations for both processes,

our calculated initial ice crystal numbers per contrail length agree well with in situ measurements over central Europe (Bräuer et al., 2021b; Febvre et al., 2009; Jessberger et al., 2013; Schumann et al., 2013) when accounting for the variability in present-day soot number emissions.

While our simulated contrail cirrus microphysical and optical properties show a similar distribution in the northern extratropics as the study by Bock and Burkhardt (2016a), there are two basic differences in our results: The first one is that we generally calculate a significantly lower ice crystal number per contrail length at initialization time (product of apparent ice number emission index and aircraft fuel consumption) in the extratropical main air traffic areas than the one resulting from the assumptions on initial ice crystal number concentration and contrail cross-sectional area made by Bock and Burkhardt (2016a). This leads in our present study to a decrease in contrail cirrus optical depth, coverage, and RF relative to the Bock and Burkhardt (2016a) results. This highlights the need to make consistent assumptions about the two quantities that are often used for initialization of contrails within models. The second difference is that in our study contrail ice nucleation is limited by atmospheric temperatures near the contrail formation threshold in particular in the tropics and subtropics leading to a significantly lower apparent ice number emission index, lower contrail cirrus ice number concentrations, and optical depth than in Bock and Burkhardt (2016a). Mainly for these two reasons, we calculate a global mean contrail cirrus RF of around 44 mWm^{-2} for the year 2006, 22% lower than the estimate of Bock and Burkhardt (2016a) for the same year. We assume a present-day soot number emission index of $1.5 \cdot 10^{15}$ kg-fuel^{-1} in our study. Since measurements imply a high variability in current engine soot number emissions behind commercial aircraft, we estimate the RF to range between around 31 mWm^{-2} (-30%) and 49 mWm^{-2} ($+12\%$) when varying soot number emissions between -66% and $+100\%$.

Hence, the RF estimate of Bock and Burkhardt (2016a) lies outside our uncertainty range resulting from the variability in soot number emissions. The RF is a function of the ice crystal number per contrail length (Burkhardt et al., 2018). Since our ice crystal numbers per contrail length agree reasonably well with observations, we conclude that our RF estimate is likely to be more realistic than the significantly higher estimate of Bock and Burkhardt (2016a). Nevertheless, it is difficult to make a conclusive judgment since only a rather limited number of observations is available that allows the determination of the apparent ice number emission index or ice crystal number per contrail length. This highlights the need for more observations that provide consistent measurement data of ice crystal number concentration and plume dilution. Additionally, the soot number emission index and fuel consumption are needed for a proper evaluation.

Furthermore, we analyze the dependency of contrail cirrus RF on soot number emissions. Fewer soot particles lead to fewer but larger ice crystals due to less competition for water vapor. These larger ice crystals are more likely to survive the vortex phase than the smaller ice crystals resulting from high soot emissions. This leads to an increase in the survival fraction for lower soot number emissions (Unterstrasser, 2016). Consequently, the ice crystal loss during the vortex phase partly compensates the decrease in nucleated ice crystal numbers resulting from reduced soot number emissions.

Reducing soot number emissions by 80%, the global average ice crystal number after the vortex phase decreases at cruise altitudes by only around 70%. As in Burkhardt et al. (2018), the RF is nonlinearly dependent on the number of emitted soot particles. Mainly due to the increase in the ice crystal survival fraction for decreased ice nucleation, our calculated relative change in the RF is slightly lower than proposed by Burkhardt et al. (2018). When assuming present-day soot number emissions of $1.5 \cdot 10^{15}$ kg-fuel^{-1}, an 80% reduction of soot number emissions leads to a decrease in RF of 41% to around 26 mWm^{-2} instead of 50% as in Burkhardt et al. (2018). If the present-day soot number emission index was higher, the decrease in soot number emissions would have a smaller impact on RF.

7.1. Implications

The significant reduction in our estimate of the RF relative to Bock and Burkhardt (2016a) has implications for the multimodel estimate of the RF from Lee et al. (2021). The initialization of contrails within climate models can have a significant impact on estimates of RF and should therefore be treated with greater care in future studies of the contrail cirrus climate impact. Since all of the other model estimates used in Lee et al. (2021) are based on contrail cirrus parameterizations that differ substantially from our ECHAM5-CCMod parameterization, in particular regarding the initialization of contrails within the model, our present study can only give an indication

of the error connected with the Bock and Burkhardt (2016a) estimate. Replacing the Bock and Burkhardt (2016a) estimate by our present estimate would, therefore, lead to a reduction in the multimodel estimate of RF and ERF (Lee et al. (2021), their Figure 3) by 6% and 4%, respectively. Nevertheless, it should be pointed out that our study demonstrates that a proper evaluation of the contrail initialization in terms of ice crystal number per contrail length, or consistent estimates for the apparent ice number emission index and fuel consumption, is important for reducing the uncertainty of the estimates of RF.

Furthermore, our study has implications for mitigation efforts reducing the climate impact of contrail cirrus. Contrail formation at lower atmospheric levels is connected with reduced ice crystal numbers after the vortex phase causing lower optical thickness, shorter contrail cirrus lifetimes, and leading to a lower radiative impact (Burkhardt et al., 2018). Therefore, any change in the cruise altitude of the aircraft can change contrail cirrus properties and radiative impact even if contrail formation is still possible.

Finally, Burkhardt et al. (2018) clarified that large reductions in initial contrail ice crystal numbers are necessary in order to obtain a significant decrease in the RF. Our study emphasizes that soot number emission reductions need to be even higher to reach the same mitigation effect because the decreased ice crystal loss in the vortex phase partly compensates for the reduced ice nucleation.

7.2. Remaining Uncertainties and Outlook

We have reduced the uncertainty of contrail cirrus RF caused by the uncertainty in the microphysical properties within young contrails and give an uncertainty range in contrail cirrus RF that is associated with the variability in soot number emissions. Nevertheless, a large uncertainty in the contrail cirrus climate impact remains. Additional uncertainties, for example, connected with the ice crystal habit, vertical cloud overlap, cloud inhomogeneities, and the radiative response to many very small ice crystals (Bock & Burkhardt, 2016a) lead to a large uncertainty in the radiative impact of contrail cirrus (Lee et al., 2021). Furthermore, biases in the background fields of meteorological variables, for example, the upper tropospheric temperature and humidity, in particular ice supersaturation, natural clouds, and their properties and the modification of natural clouds in the presence of contrail cirrus (Bickel et al., 2020), lead to uncertainties in the contrail cirrus RF. These uncertainties are unlikely to be resolved in the near future since the uncertainties connected with natural cloud properties are longstanding (Stevens & Bony, 2013). Recently, many cloud related variables such as precipitation features, cloud vertical structure, cloud sizes, and daily cycles were shown to be improved in storm-resolving simulations (Stevens et al., 2020) but uncertainties connected with the cloud microphysical schemes remain. Further improvements can be expected if future
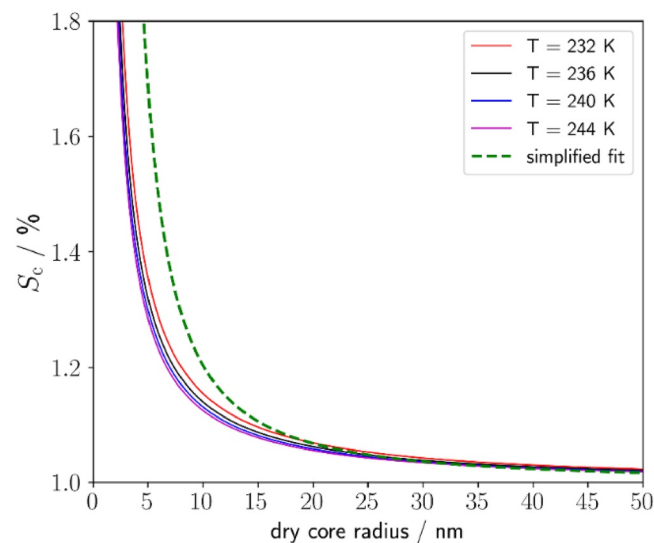

Figure 9. Critical saturation ratio (S_c) for activation of soot particles depending on their dry core radii for different plume temperatures (T) calculated as the maximum of the Kappa-Köhler Equation 6 from Petters and Kreidenweis (2007) by applying Newtonian Iteration. The green dashed line shows the result for S_c when using the simplified Equation 10 from Petters and Kreidenweis (2007).

contrail cirrus studies can utilize the progress in storm-resolving modeling not only in regional studies (Verma & Burkhardt, 2022) but also on the global scale.

Appendix A: Modification of Contrail Ice Nucleation Parameterization

Kärcher et al. (2015) use the Kappa-Köhler theory according to Petters and Kreidenweis (2007), abbreviated as PK2007 hereafter, to calculate the activation dry core radius for soot ($r_{d,act,s}$) and for entrained ambient particles ($r_{d,act,s}$) at a given plume saturation ratio S_p so that all soot (ambient) particles with dry core radii $r_{d,s} \geq r_{d,act,s}$ ($r_{d,a} \geq r_{d,act,a}$) will activate into water droplets. Note that in this method and as soon as the plume becomes supersaturated, S_p is effectively considered as a critical saturation ratio S_c (maximum of the Köhler curve) and $r_{d,act}$ is calculated as the corresponding dry core radius to S_c. The dependency between S_p and $r_{d,act}$ (or rather S_c and r_d) basically depends on the hygroscopicity parameter κ. Assuming a soluble volume fraction of 1%, Kärcher et al. (2015) prescribe the hygroscopicity of soot κ_s with 0.005 and set the solubility of ambient particles κ_a to 0.5.

In the ice nucleation parameterization of Kärcher et al. (2015), the simplified fit Equation 10 from PK2007 is used to calculate $r_{d,act}$ although this expression is just valid for $\kappa >\approx 0.1$ making its use appropriate for ambient particles. We modify the parameterization by applying the full Kappa-Köhler equation (Equation 6 from PK2007) to soot particles, keeping $\kappa_s = 0.005$, and determine S_c depending on $r_{d,s}$ by Newtonian Iteration (Appendix B of Bier et al., 2022). Figure 9 displays our calculated S_c for different plume temperatures, where typically droplet activation occurs, and that obtained from Equation 10 from PK2007. S_c in general rises with decreasing $r_{d,s}$ with an enhanced increase for small dry core radii (below 10 nm) due to the stronger Kelvin effect. In general, the temperature dependency is relatively low and S_c increases with decreasing T for a given dry core size. The dashed line shows that the simplified fit equation overestimates S_c for $r_{d,s}$ below 15 nm. This overestimation strongly increases with decreasing $r_{d,s}$. This means that the number of formed contrail ice crystals will be clearly overestimated at higher plume supersaturations if the simplified fit is used. This will impact the contrail ice nucleation in the subtropics and extratropics (as described in Section 4.1).

We derive an expression for the activation dry core radius of soot particles depending on the plume saturation ration (S_p) based on P. & K. (6). We set T to 236 K which is a typical exhaust temperature in the extratropical cruise altitudes when droplet formation occurs. In near-threshold cases (i.e., particularly in the tropics), droplet formation occurs later and, therefore, at lower plume temperature. But since only the larger soot particles can activate into water droplets at those conditions and S_c hardly varies with T for higher $r_{d,act,s}$, fixing T leads to a negligible error. The relation of S_c versus $r_{d,s}$ is equivalent to the relation of S_p versus $r_{d,act,s}$ (Kärcher et al., 2015). Solving for $r_{d,act,s}$ (black line of Figure 9), we determine the following fit formula:

$$r_{d,act,s} / \text{nm} = a_0 + a_1 \ln^{-1}(S_p) + a_2 \ln^{-2}(S_p) + a_3 \ln^{-3}(S_p) + a_4 \ln^{-4}(S_p). \tag{A1}$$

We restrict the range of calculated dry core radii to $1 \text{ nm} < r_{d,act,s} < 150 \text{ nm}$ which in sum contains almost all (>99.9%) soot particles while assuming the same log-normal size distribution as in Kärcher et al. (2015). We set $r_{d,act,s}$ to 150 nm for $S_p < 1.005$ and to 1 nm for $S_p > 4.5$. The fit parameters are $a_0 = 0.96453426$, $a_1 = 1.21152973$, $a_2 = -0.00520358$, $a_3 = 2.32286432 * 10^{-5}$, and $a4 = -4.36979055 * 10^{-8}$ and the correlation coefficient to the black line of Figure 9 equals to 0.9999938. Finally, we replace the equation for $r_{d,act,s}$ from the parameterization of Kärcher et al. (2015) by our Equation A1 but keep the original fit formula for the ambient particles accounting for the correction of the transcription error described in Bier and Burkhardt (2019).

Table 1 are taken from the COLI data set (Schumann et al., 2017) and Bräuer et al. (2021b). The presented data, on which our Figures are based, are available in the zenodo repository at https://zenodo.org/record/6902742 and licensed under Creative Commons Attribution 3.0 Germany. Figures 2 and 9 have been created with the data analysis and scientific visualization tool QtiPlot (see https://www.qtiplot.com). Global distributions and vertical profiles (Figures 3–8b) are visualized with Ferret, which is a product of the NOAA's Pacific Marine Environmental Laboratory (information available at http://ferret.pmel.noaa.gov/Ferret/). Figure 8c was created with Python 3.6 (van Rossum, 2018).

References

Anderson, B. E., Cofer, W. R., Bagwell, D. R., Barrick, J. W., Hudgins, C. H., & Brunke, K. E. (1998). Airborne observations of aircraft aerosol emissions I: Total nonvolatile particle emission indices. *Geophysical Research Letters*, *25*(10), 1689–1692. https://doi.org/10.1029/98gl00063

Bickel, M., Ponater, M., Bock, L., Burkhardt, U., & Reineke, S. (2020). Estimating the effective radiative forcing of contrail cirrus. *Journal of Climate*, *33*(5), 1991–2005. https://doi.org/10.1175/JCLI-D-19-0467.1

Bier, A., & Burkhardt, U. (2019). Variability in contrail ice nucleation and its dependence on soot number emissions. *Journal of Geophysical Research: Atmospheres*, *124*(6), 3384–3400. https://doi.org/10.1029/2018JD029155

Bier, A., Burkhardt, U., & Bock, L. (2017). Synoptic control of contrail cirrus life cycles and their modification due to reduced soot number emissions. *Journal of Geophysical Research: Atmospheres*, *122*(21), 11584–11603. https://doi.org/10.1002/2017JD027011

Bier, A., Unterstrasser, S., & Vancassel, X. (2022). Box model trajectory studies of contrail formation using a particle-based cloud microphysics scheme. *Atmospheric Chemistry and Physics*, *22*(2), 823–845. https://doi.org/10.5194/acp-22-823-2022

Bock, L., & Burkhardt, U. (2016a). Reassessing properties and radiative forcing of contrail cirrus using a global climate model. *Journal of Geophysical Research: Atmospheres*, *121*(16), 9717–9736. https://doi.org/10.1002/2016JD025112

Bock, L., & Burkhardt, U. (2016b). The temporal evolution of a long-lived contrail cirrus cluster: Simulations with a global climate model. *Journal of Geophysical Research: Atmospheres*, *121*(7), 3548–3565. https://doi.org/10.1002/2015JD024475

Bock, L., & Burkhardt, U. (2019). Contrail cirrus radiative forcing for future air traffic. *Atmospheric Chemistry and Physics*, *19*(12), 8163–8174. https://doi.org/10.5194/acp-19-8163-2019

Boucher, O., Randall, D., Artaxo, P., Bretherton, C., Feingold, G., Forster, P., et al. (2013). Clouds and aerosols. In T. Stocker, D. Qin, G. K. Plattner, M. M. B. Tignor, S. K. Allen, J. Boschung, et al. (Eds.) *Climate change 2013: The physical science basis. Contribution of working group I to the fifth assessment report of the intergovernmental panel on climate change* (Vol. 7, pp. 571–658). Cambridge University Press.

Bräuer, T., Voigt, C., Sauer, D., Kaufmann, S., Hahn, V., Scheibe, M., et al. (2021a). Airborne measurements of contrail ice properties—Dependence on temperature and humidity. *Geophysical Research Letters*, *1*(8), e2020GL092166. https://doi.org/10.1029/2020gl092166

Bräuer, T., Voigt, C., Sauer, D., Kaufmann, S., Hahn, V., Scheibe, M., et al. (2021b). Reduced ice number concentrations in contrails from low-aromatic biofuel blends. *Atmospheric Chemistry and Physics*, *21*(22), 16817–16826. https://doi.org/10.5194/acp-21-16817-2021

Burkhardt, U., Bock, L., & Bier, A. (2018). Mitigating the contrail cirrus climate impact by reducing aircraft soot number emissions. *Npj Climate and Atmospheric Science*, *37*, 1–7. https://doi.org/10.1029/2008GL034056

Burkhardt, U., & Kärcher, B. (2009). Process-based simulation of contrail cirrus in a global climate model. *Journal of Geophysical Research*, *114*(D16), D16201. https://doi.org/10.1029/2008JD011491

Burkhardt, U., & Kärcher, B. (2011). Global radiative forcing from contrail cirrus. *Nature Climate Change*, *1*(1), 54–58. https://doi.org/10.1038/NCLIMATE1068

Burkhardt, U., Kärcher, B., Ponater, M., Gierens, K., & Gettelman, A. (2008). Contrail cirrus supporting areas in model and observations. *Geophysical Research Letters*, *35*(16), L16808. https://doi.org/10.1029/2008GL034056

Chen, C.-C., & Gettelman, A. (2013). Simulated radiative forcing from contrails and contrail cirrus. *Atmospheric Chemistry and Physics*, *13*(24), 12525–12536. https://doi.org/10.5194/acp-13-12525-2013

Eyers, C., Norman, P., Middel, J., Plohr, M., Michot, S., Atkinson, K., & Christou, R. (2004). *AERO2K global aviation emissions inventories for 2002 and 2025* (Technical Report QINETIC/04/01113). QinetiQ.

Febvre, G., Gayet, J., Minikin, A., Schlager, H., Shcherbakov, V., Jourdan, O., et al. (2009). On optical and microphysical characteristics of contrails and cirrus. *Journal of Geophysical Research*, *114*(D2), D02204. https://doi.org/10.1029/2008JD010184

Freudenthaler, V., Homburg, F., & Jäger, H. (1995). Contrail observations by ground-based scanning lidar: Cross-sectional growth. *Geophysical Research Letters*, *22*(24), 3501–3504. https://doi.org/10.1029/95gl03549

Gerz, T., Duerbeck, T., & Konopka, P. (1998). Transport and effective diffusion of aircraft emissions. *Journal of Geophysical Research*, *103*(D20), 25905–25913. https://doi.org/10.1029/98jd02282

Gierens, K., & Bretl, S. (2009). Analytical treatment of ice sublimation and test of sublimation parameterisations in two-moment ice microphysics models. *Atmospheric Chemistry and Physics*, *9*(19), 7481–7490. https://doi.org/10.5194/acp-9-7481-2009

Hansen, J. E., & Travis, L. D. (1974). Light scattering in planetary atmospheres. *Space Science Reviews*, *16*(4), 527–610. https://doi.org/10.1007/bf00168069

International Civil Aviation Organization. (2013). Environmental report 2013—aviation and climate change, Montreal, Canada.

Jessberger, P., Voigt, C., Schumann, U., Sölch, I., Schlager, H., Kaufmann, S., et al. (2013). Aircraft type influence on contrail properties. *Atmospheric Chemistry and Physics*, *13*(23), 11965–11984. https://doi.org/10.5194/acp-13-11965-2013

Kärcher, B. (2018). Formation and radiative forcing of contrail cirrus. *Nature Communications*, *9*(1), 1824. https://doi.org/10.1038/s41467-018-04068-0

Kärcher, B., Burkhardt, U., Bier, A., Bock, L., & Ford, I. J. (2015). The microphysical pathway to contrail formation. *Journal of Geophysical Research: Atmospheres*, *120*(15), 7893–7927. https://doi.org/10.1002/2015JD023491

Kärcher, B., Burkhardt, U., Unterstrasser, S., & Minnis, P. (2009). Factors controlling contrail cirrus optical depth. *Atmospheric Chemistry and Physics*, *9*(16), 6229–6254. https://doi.org/10.5194/acp-9-6229-2009

Kärcher, B., & Yu, F. (2009). Role of aircraft soot emissions in contrail formation. *Geophysical Research Letters*, *36*(1), L01804. https://doi.org/10.1029/2008GL036649

Kurz, C. (2007). *Entwicklung und Anwendung eines gekoppelten Klima-Chemie-Modellsystems: Globale Spurengastransporte und chemische Umwandlungsprozesse* (Doctoral thesis). Ludwigs-Maximilians-University Munich, DLR Forschungsbericht 2007–2012.

Lee, D. S., Fahey, D. W., Skowron, A., Allen, M. R., Burkhardt, U., Chen, Q., et al. (2021). The contribution of global aviation to anthropogenic climate forcing for 2010 to 2018. *Atmospheric Environment*, *244*, 117834. https://doi.org/10.1016/j.atmosenv.2020.117834

Lewellen, D., & Lewellen, W. (2001). The effects of aircraft wake dynamics on contrail development. *Journal of the Atmospheric Sciences*, *58*(4), 390–406. https://doi.org/10.1175/1520-0469(2001)058<0390:teoawd>2.0.co;2

Lohmann, U., Spichtinger, P., Heidt, S., Peter, T., & Smit, H. (2008). Cirrus clouds and ice supersaturation regions in a global climate model. *Environmental Research Letters*, *3*(4), 045022. https://doi.org/10.1088/1748-9326/3/4/045022

Moore, R. H., Thornhill, K. L., Weinzierl, B., Sauer, D., D'Ascoli, E., Kim, J., et al. (2017). Biofuel blending reduces particle emissions from aircraft engines at cruise conditions. *Nature*, *543*(7645), 411–415. https://doi.org/10.1038/nature21420

Paoli, R., & Shariff, K. (2016). Contrail modeling and simulation. *Annual Review of Fluid Mechanics*, *48*(1), 393–427. https://doi.org/10.1146/annurev-fluid-010814-013619

Petters, M. D., & Kreidenweis, S. M. (2007). A single parameter representation of hygroscopic growth and cloud condensation nucleus activity. *Atmospheric Chemistry and Physics*, *7*(8), 1961–1971. https://doi.org/10.5194/acp-7-1961-2007

Petzold, A., Döpelheuer, A., Brock, C. A., & Schröder, F. (1999). In situ observations and model calculations of black carbon emission by aircraft at cruise altitude. *Journal of Geophysical Research*, *104*(D18), 22171–22181. https://doi.org/10.1029/1999jd900460

Ponater, M., Bickel, M., Bock, L., & Burkhardt, U. (2021). Towards determining the contrail cirrus efficacy. *Aerospace*, *8*(2), 42. https://doi.org/10.3390/aerospace8020042

Roeckner, E., Baeuml, G., Bonaventura, L., Brokopf, R., Esch, M., Giorgetta, M., et al. (2003). The atmospheric general circulation model ECHAM5. Part 1: Model description, Max-Planck-Institute Report (Vol. *349*, p. 127).

Roeckner, E., Brokopf, R., Esch, M., Giorgetta, M., Hagemann, S., Kornblueh, L., et al. (2006). Sensitivity of simulated climate to horizontal and vertical resolution in the ECHAM5 atmosphere model. *Journal of Climate*, *19*(16), 3771–3791. https://doi.org/10.1175/jcli3824.1

Schumann, U. (1996). On conditions for contrail formation from aircraft exhausts. *Meteorologische Zeitschrift*, *5*(1), 4–23. https://doi.org/10.1127/metz/5/1996/4

Schumann, U. (2012). A contrail cirrus prediction model. *Geoscience Model Development*, *5*(3), 543–580. https://doi.org/10.5194/gmd-5-543-2012

Schumann, U., Arnold, F., Busen, R., Curtius, J., Kärcher, B., Kiendler, A., & Wohlfrom, K. H. (2002). Influence of fuel sulfur on the composition of aircraft exhaust plumes: The experiments SULFUR 1–7. *Journal of Geophysical Research*, *107*, D15. https://doi.org/10.1029/2001JD000813

Schumann, U., Baumann, R., Baumgardner, D., Bedka, S. T., Duda, D. P., Freudenthaler, V., et al. (2017). Properties of individual contrails: A compilation of observations and some comparisons. *Atmospheric Chemistry and Physics*, *17*(1), 403–438. https://doi.org/10.5194/acp-17-403-2017

Schumann, U., & Heymsfield, A. (2017). On the lifecycle of individual contrails and contrail cirrus. *Meteorological Monographs*, *58*, 3-1–3-24. https://doi.org/10.1175/AMSMONOGRAPHS-D-16-0005.1

Schumann, U., Jeßberger, P., & Voigt, C. (2013). Contrail ice particles in aircraft wakes and their climatic importance. *Geophysical Research Letters*, *40*(11), 2867–2872. https://doi.org/10.1002/grl.50539

Schumann, U., Penner, J. E., Chen, Y., Zhou, C., & Graf, K. (2015). Dehydration effects from contrails in a coupled contrail-climate model. *Atmospheric Chemistry and Physics*, *15*(19), 11179–11199. https://doi.org/10.5194/acp-15-11179-2015

Schumann, U., Schlager, H., Arnold, F., Baumann, R., Haschberger, P., & Klemm, O. (1998). Dilution of aircraft exhaust plumes at cruise altitudes. *Atmospheric Environment*, *32*(18), 3097–3103. https://doi.org/10.1016/s1352-2310(97)00455-x

Smolarkiewicz, P. K., & Grell, P. A. (1992). A class of monotone interpolation schemes. *Journal of Computational Physics*, *101*(2), 431–440. https://doi.org/10.1016/0021-9991(92)90018-T

Sölch, I., & Kärcher, B. (2010). A large-eddy model for cirrus clouds with explicit aerosol and ice microphysics and Lagrangian ice particle tracking. *Quarterly Journal of the Royal Meteorological Society*, *136*(653), 2074–2093. https://doi.org/10.1002/qj.689

Stevens, B., Acquistapace, C., Hansen, A., Heinze, R., Klinger, C., Klocke, D., et al. (2020). The added value of large-eddy and storm-resolving models for simulating clouds and precipitation. *Journal of Meteorological Society of Japan*, *98*(2), 395–435. https://doi.org/10.2151/jmsj.2020-021

Stevens, B., & Bony, S. (2013). What are climate models missing? *Science*, *340*(6136), 1053–1054. https://doi.org/10.1126/science.1237554

Stier, P., Feichter, J., Kinne, S., Kloster, S., Vignati, E., Wilson, J., et al. (2005). The aerosol-climate model ECHAM5-HAM. *Atmospheric Chemistry and Physics*, *5*(4), 1125–1156. https://doi.org/10.5194/acp-5-1125-2005

Stuber, N., Sausen, R., & Ponater, M. (2001). Stratosphere adjusted radiative forcing calculations in a comprehensive climate model. *Theoretical and Applied Climatology*, *68*(3–4), 125–135. https://doi.org/10.1007/s007040170041

Sussmann, R., & Gierens, K. (1999). Lidar and numerical studies on the different evolution of vortex pair and secondary wake in young contrails. *Journal of Geophysical Research*, *104*(D2), 2131–2142. https://doi.org/10.1029/1998jd200034

Taylor, K. E., Williamson, D., & Zwiers, F. (2000). *The sea surface temperature and sea-ice concentration boundary conditions for AMIP II simulations, PCMDI report no. 60, program for climate model diagnostics and intercomparison*. University of California, Lawrence Livermore National Laboratory.

Unterstrasser, S. (2014). Large eddy simulation study of contrail microphysics and geometry during the vortex phase and consequences on contrail-to-cirrus transition. *Journal of Geophysical Research: Atmospheres*, *119*(12), 7537–7555. https://doi.org/10.1002/2013JD021418

Unterstrasser, S. (2016). Properties of young contrails—A parametrisation based on large-eddy simulations. *Atmospheric Chemistry and Physics*, *16*(4), 2059–2082. https://doi.org/10.5194/acp-16-2059-2016

Unterstrasser, S., & Gierens, K. (2010). Numerical simulations of contrail-to-cirrus transition—Part 2: Impact of initial ice crystal number, radiation, stratification, secondary nucleation and layer depth. *Atmospheric Chemistry and Physics*, *10*(4), 2037–2051. https://doi.org/10.5194/acp-10-2037-2010

Unterstrasser, S., & Görsch, N. (2014). Aircraft-type dependency of contrail evolution. *Journal of Geophysical Research*, *119*(24), 14015–14027. https://doi.org/10.1002/2014JD022642

van Rossum, G. (2018). *Python tutorial: Release 3.6.6rc1 (Software)*. Python Software Foundation.

Verma, P., & Burkhardt, U. (2022). Contrail formation within cirrus: ICON-LEM simulations of the impact of cirrus cloud properties on contrail formation. *Atmospheric Chemistry and Physics*, *22*(13), 8819–8842. https://doi.org/10.5194/acp-22-8819-2022

Wilkerson, J. T., Jacobson, M. Z., Malwitz, A., Balasubramanian, S., Wayson, R., Fleming, G., et al. (2010). Analysis of emission data from global commercial aviation: 2004 and 2006. *Atmospheric Chemistry and Physics*, *10*(13), 6391–6408. https://doi.org/10.5194/acp-10-6391-2010